A new accurate retrieval of bromine monoxide inside minor volcanic plumes from Sentinel-5 Precursor/TROPOMI

Simon Warnach[1,4], Holger Sihler[5], Christian Borger[1], Nicole Bobrowski[2,3], Steffen Beirle[1], Ulrich Platt[2], and Thomas Wagner[1]

[1]Max-Planck-Institut für Chemie (MPIC), Satellite remote sensing group, Mainz, Germany
[2]Institut für Umweltphysik (IUP), Heidelberg University, Heidelberg, Germany
[3]Istituto Nazionale di Geofisica e Vulcanologia - Osservatorio Etneo, Catania, Italy
[4]now at Laboratoire de Physique et de Chimie de l'Environnement et de l'Espace (LPC2E), CNRS, Université d'Orléans, Orléans, France
[5]formerly at: Max-Planck-Institut für Chemie (MPIC), Satellite remote sensing group, Mainz, Germany

Correspondence: Simon Warnach (s.warnach@mpic.de)

Abstract. Bromine monoxide (BrO) is a key radical in the atmosphere, influencing the chemical state of the atmosphere, most notably the abundance of ozone. The main effect of BrO onto tropospheric ozone concentrations occurs in bromine release events in polar regions, salt pans and volcanic plumes. Ozone depletion caused by halogen release has been observed and modeled for such conditions, in particular inside volcanic plumes. Furthermore, the molar bromine to sulphur ratio in volcanic plumes is a proxy for the magmatic composition of a volcano and potentially an eruption forecast parameter. The integrated column of BrO in the atmosphere, which in turn serves as an estimate for the bromine content, can be detected simultaneously with SO_2 via spectroscopic measurements using the Differential Optical Absorption Spectroscopy (DOAS). Thus, a direct derivation of the BrO/SO_2 ratio can be performed from a single measurement.

Satellite spectroscopic observations offer the potential to observe and monitor volcanic bromine release globally. The detection of BrO in volcanic plumes is limited by the precision and sensitivity of the retrieval, which so far only allowed for the detection of BrO during major eruptions, leading to a potential sampling bias when looking at the BrO/SO_2 ratio. The The TROPospheric Monitoring Instrument (TROPOMI) onboard Sentinel-5 Precursor (S-5P) however, with its unprecedented spatial resolution of up to $3.5 \times 5.5\,km^2$ and high signal-to-noise ratio, enables the detection of BrO in minor eruptions or even quiescent degassing.

In this study, we investigate, how far the BrO retrieval can be improved using TROPOMI data and how well BrO can be detected, even in small eruptions and during quiescent volcanic degassing. There are two steps, for which improvements in accuracy are investigated and applied: the improvement and quantitative determination of (1) the detection limit of the DOAS BrO column retrieval and (2) the correction of non-volcanic background BrO signal. First, the DOAS retrieval settings are varied and their influence on accuracy and precision is investigated with respect to the detection limit and potential systematic influences. Based on these results, we propose a dedicated DOAS evaluation scheme optimized for the detection of BrO in volcanic plumes. For the DOAS retrieval, we propose the use of a large fit window from $323 - 360\,nm$, yielding a factor of 1.8 lower statistical uncertainty compared to previous BrO DOAS algorithms, while not enhancing systematic influences.

Second, the effect of the background BrO is reduced by a latitude dependent empirical correction scheme correlated to cloud information as well as information on the ozone column. Via these improvements, the combined statistical and systematic

25 uncertainties of the resulting BrO vertical column density is in the order of $7 \times 10^{12}\,\mathrm{molecules\,cm^{-2}}$, which allows for the detection of even slightly enhanced BrO amounts inside minor eruptive plumes of bromine-rich volcanoes.

1 Introduction

Bromine monoxide (BrO) has been found to be a catalyst for ozone (O_3) destruction (e. g. in the polar regions, see Barrie et al., 1988; Simpson et al., 2007). Volcanic bromine release is thought to also affect atmospheric ozone chemistry (von

30 Glasow, 2010; Surl et al., 2021), and strong eruptions ejecting bromine into the tropical stratosphere can potentially impact global stratospheric ozone abundance over a ten-year period (Brenna et al., 2019). BrO in volcanic plumes was first detected at Soufriere Hills (Bobrowski et al., 2003) using ground-based Differential Optical Absorption Spectroscopic (DOAS, Perner and Platt, 1979) measurements. BrO and SO_2, which can be detected by DOAS simultaneously, have been measured over the last 20 years at many volcanoes using ground-based instruments and the BrO/SO_2 ratio has proven to be a useful tool both to

35 determine the composition of a volcanic plume (Bobrowski and Platt, 2007; Kern et al., 2009; Hörmann et al., 2013) as well as a proxy for changes in the volcanic system (Bobrowski and Giuffrida, 2012; Lübcke et al., 2014; Bobrowski et al., 2015; Dinger et al., 2018; Warnach et al., 2019).

After the unsuccessful attempt to detect BrO in volcanic plumes using satellite data from GOME and SCIAMACHY (Afe et al., 2004), volcanic BrO was first detected from GOME-2 in the plume of Kasatochi in 2008 by Theys et al. (2009). A global

40 detection algorithm of BrO and the BrO/SO_2 ratios inside volcanic plumes from GOME-2 was developed by Hörmann et al. (2013).

DOAS retrievals of BrO from satellites have varied over time, both w. r. t. the wavelength fit range as well as other DOAS fit settings. The first detection of tropospheric BrO from the GOME instrument by Wagner and Platt (1998), employs a wavelength range of $345 - 359.5\,\mathrm{nm}$. Other studies use almost identical fit ranges for spectra from GOME (Richter et al., 1998; Hegels

45 et al., 1998; Chance, 1998; Richter et al., 2002) and for spectra from OMI (Chance, 2002). For SCIAMACHY and GOME-2 measurements, the short wavelength limit of the fit range was lowered to $336\,\mathrm{nm}$, and the upper limit varied between $347\,\mathrm{nm}$ (Afe et al., 2004; Begoin et al., 2010), $351 - 352\,\mathrm{nm}$ (Valks et al., 2009; Theys et al., 2009), and $360\,\mathrm{nm}$ (Heue et al., 2011; Sihler et al., 2012; Hörmann et al., 2013). The short wavelength limit of $336\,\mathrm{nm}$ was also found best in a long-term study combining GOME, SCIAMACHY, and GOME-2 measurments (Bougoudis et al., 2020). For recent global studies of BrO

50 from GOME-2 (Theys et al., 2011) and TROPOMI (Seo et al., 2019) the lower boundary was further lowered and a fit range of $332 - 359\,\mathrm{nm}$ and $334.6 - 358\,\mathrm{nm}$ was chosen respectively.

The DOAS BrO fit used in this study is based on the BrO fit developed by Sihler et al. (2012) for the retrieval of BrO in arctic regions, which was also used for the detection of BrO in volcanic plumes by Hörmann et al. (2013). There, a fit range from $336 - 360\,\mathrm{nm}$ was chosen. The omission of shorter wavelengths was mainly attributed to the strong ozone absorption in

55 the UV at high latitudes, caused by the large ozone columns and high solar zenith angles (SZAs).

In this study, we report on the further improvement of the BrO DOAS retrieval with a specific focus on the detection of BrO in volcanic plumes and propose a new accurate BrO retrieval for the detection within minor volcanic plumes. Retrieval improvements are investigated by varying the DOAS fit settings, by both considering lower wavelengths and the inclusion/exclusion of the formaldehyde (HCHO) cross section in the DOAS fit. The aim of this task was to achieve both a low statistical uncertainty and low systematic errors, especially low interferences caused by clouds, ozone and HCHO.

There are several reasons why - in contrast to previous retrievals - lower wavelengths can be included in current BrO DOAS retrievals for the detection of volcanic plumes. First, the introduction of the so-called Pukite terms (Puķīte et al., 2010) can largely compensate the spectral effects of the strong ozone absorption. Second, volcanic plumes mainly occur at lower latitudes, where ozone columns and the SZAs are considerably lower compared to high latitudes. Third, the use of an earthshine reference spectrum recorded at the equator reduces the optical density of ozone to zero at the equator, further reducing the potential ozone interference at low latitudes.

The question whether it is advantageous to include HCHO in the BrO DOAS fit is long debated, as the interference between BrO and HCHO is a well known difficulty both in BrO and HCHO DOAS retrievals (Theys et al., 2011; Vogel et al., 2013; De Smedt et al., 2018). The structure of the absorption cross-section of BrO and HCHO are very similar (cf. Fig. 1). Especially the fact, that the largest absorption peak of BrO overlaps with a major absorption peak of HCHO at $339\,\text{nm}$, can cause a spectral interference between both trace gases. For arctic applications, such as Wagner and Platt (1998), Richter et al. (1998), but also for the more recent study by Sihler et al. (2012), HCHO was not included as an absorber in the DOAS retrieval, because HCHO is almost not abundant in arctic regions. However, in equatorial regions, where HCHO can reach high column densities due to biogenic emissions or biomass burning, spectral interference with HCHO can become important. HCHO is therefore included within the DOAS analysis of the global BrO detection algorithms of GOME-2 by Theys et al. (2011) and the TROPOMI algorithm of polar BrO by Seo et al. (2019). Interferences between BrO and HCHO are observed for equatorial regions by Theys et al. (2011). Using $332\,\text{nm}$ compared to $336\,\text{nm}$ (used in Sihler et al., 2012) as the lower fit boundary reduces these interferences (Theys et al., 2011). Hence, both Theys et al. (2011) and Seo et al. (2019) employ fit ranges with a lower wavelength limit of $332\,\text{nm}$ and $334.6\,\text{nm}$ respectively.

The stratospheric background of BrO together with the potential BrO background of the free troposphere is up to one order of magnitude larger than volcanic BrO columns of small eruptions. Therefore, an imperfect subtraction of the background column can yield uncertainties in the order of small volcanic signals. Hence, an accurate background correction is essential. Fortunately, horizontal gradients of the stratospheric BrO VCD occur on a much larger scale than the extension of volcanic plumes. Moreover, while stratospheric gradients mainly originate from changes in the tropopause height (Sihler et al., 2012), volcanic plumes are dispersions of point sources. Thus, the patterns are spatially independent from each other and a separation can be achieved by the application of a spatial high-pass filter. Moreover, volcanic plumes can be independently detected due to their enhanced SO_2 column density. Background correction on this basis was for example implemented by Hörmann et al. (2013) by first masking the volcanic plume, which is well detectable via the SO_2 signal, and subtracting a 2D polynomial fitted to the area around the volcanic plume.

90   While our BrO DOAS retrieval is in principle applicable to the complete globe, similar to the retrievals presented in Theys et al. (2011); Sihler et al. (2012); Seo et al. (2019), it is specifically optimized for the most accurate detection of BrO originating from volcanic plumes, which are local/regional events whose spatial extent is typically of the order of $10 - 100\,\mathrm{km}$, only rarely exceeding $1000\,\mathrm{km}$.

    This paper is structured as follows: in Sect. 2, we describe the TROPOMI instrument and the basics of our BrO DOAS
95   retrieval from satellite. The investigation of different DOAS fit settings is described in Sect. 3. For these fit settings the systematic influence of clouds, ozone and HCHO are discussed, corrected, and the remaining systematic influences are quantified in Sect. 4. In combination with an investigation of the statistical uncertainties (Sect. 5.1), the most suitable fit settings for an accurate retrieval within minor volcanic plumes is proposed in Sect. 5. The proposed retrieval algorithm is tested on multiple volcanic plumes of different emission strengths and at different latitudes in Sect. 6 to demonstrate its accuracy and efficacy.
100   Lastly, conclusions are drawn in Sect. 7.

2 Methods

2.1 The TROPOMI instrument

The TROPospheric Monitoring Instrument (TROPOMI, Veefkind et al., 2012) is onboard the satellite Sentinel-5 precursor (S-5P) of the European Space Agency (ESA). S-5P is a sun-synchronous, polar-orbiting satellite with an orbital inclination of
105   $98.7°$ on a low-Earth orbit (altitude: $824\,\mathrm{km}$) launched on 13 October 2017. Its equator crossing time is roughly at $13:30\,\mathrm{h}$ mean local solar time and it has a repeat cycle of 17 days. S-5P and its single payload TROPOMI are designed to determine and monitor the atmospheric composition. TROPOMI uses a push-broom method to scan the Earth's surface. The opening angle of $108°$ leads to a ground swath of approx. $2600\,\mathrm{km}$ (separated to 450 pixels) and allows for an almost complete daily coverage of the whole globe.
110   TROPOMI is a hyperspectral imaging spectrometer measuring radiance spectra via four different detectors in the ultra-violett $270 - 320\,\mathrm{nm}$ (UV), UV-visible $310 - 500\,\mathrm{nm}$ (UVIS), near-infrared $675 - 775\,\mathrm{nm}$ (NIR), and short-wave-infrared $2305 - 2385\,\mathrm{nm}$ (SWIR). A detailed overview of the spectral characteristica for each detector is given in Veefkind et al. (2012).

2.1.1 TROPOMI UVIS spectra used

For the DOAS retrieval of BrO the L1B radiance spectra from the UVIS channel are used. The UVIS channel has a along-track
115   pixel size of $7\,\mathrm{km}$, which was reduced to $5.5\,\mathrm{km}$ on 6 August 2019. There are 450 across-track pixels, whose size varies from $3.5\,\mathrm{km}$ at nadir up to $14.4\,\mathrm{km}$ at large viewing angles. Thus, the highest spatial resolution is $5.5 \times 3.5\,\mathrm{km}^2 = 19.25\,\mathrm{km}^2$.

2.1.2 Additional input data

For the investigation of systematic errors and their correction several additional input data-sets are used in this study.

First, for the investigation of the influence of clouds onto the retrieval and for its correction, there are two cloud data-
120   sets used: the cloud height (CH) and the cloud fraction (CF). Both data-sets are calculated using the FRESCO algorithm
(Compernolle et al., 2021) and provided within the NO_2 operational product (van Geffen et al., 2021; NO2, 2021). While
the cloud fraction is directly inferred within the FRESCO algorithm, the cloud height is calculated from the FRESCO cloud
pressure (CP), surface pressure (SP) and surface altitude (SA) all provided within the NO_2 product (van Geffen et al., 2021;
NO2, 2021) via the barometric pressure formula. To ensure the use of the latest FRESCO product, we used the reprocessed
125   version of the NO_2 product, provided via the sentinel-5 precursor expert hub (https://s5pexp.copernicus.eu/). For this study, we
choose the FRESCO cloud products, as they are easily accessible via the operational NO_2 product and are therefore available
for the complete TROPOMI sensing period. However, also other cloud products are available (Latsch et al., 2022) and could
in principle be used. For example the use of the cloud fractions provided by the Mainz Iterative Cloud Retrieval Utilities
(MICRU, Sihler et al., 2020) was tested in Warnach (2022) and found suitable for application within the retrieval presented
130   here. However, unfortunately it is not available for the complete TROPOMI measurement period.

Second, for the study of the influence of HCHO onto the BrO retrieval, the operational TROPOMI L2 HCHO product is
used (De Smedt et al., 2018).

Third, for the estimation of the stratospheric column strength the O_3 VCD is used. The O_3 VCD is derived directly from the
BrO DOAS fit (cf. Sect. 4.2 for a detailed description).

135   **2.2   The DOAS fitting routine**

The DOAS method was introduced by Perner and Platt (1979) and is based on the attenuation of light in the atmosphere
described by the Beer-Lambert-Bouguer law. The DOAS method makes use of the fact that molecules are distinguishable by
their unique absorption structure originating from electronic, vibrational, and rotational excitations. These structures usually
contain high frequency structures, which can be distinguished from the broad band extinction features of atmospheric scattering
140   processes such as Mie and Rayleigh scattering. Essentially, the optical density τ of the absorption of the trace gas in question
is retrieved by comparing the measurement spectrum's intensity $I(\lambda)$ with a so called «reference spectrum» $I_0(\lambda)$:

$$\tau = ln\left(\frac{I_0(\lambda)}{I(\lambda)}\right) = \sum_i \sigma_i(\lambda) \cdot \int_L c_i(l)\, dl = \sum_i \sigma_i(\lambda) \cdot SCD_i \qquad (1)$$

The result of the DOAS analysis will be the difference of the columns of the trace gases between reference and measurement
spectrum, the slant column density (SCD). DOAS thus requires only knowledge about the absorption cross-sections σ of the
145   relevant absorbing molecules. Traditional DOAS algorithms employ a combination of a linear (for the contribution of the ref.
spectra) and non-linear (for spectral shift and distortion compensation) fit in order to determine the column of the absorber.
However, for satellite applications, where huge data-sets are recorded daily, a linearisation of the non-linear DOAS fit was
developed by Beirle et al. (2013) and is used here. The fitting algorithm used here was implemented and described in detail by
Borger et al. (2020). The slant column density (SCD) retrieved in the DOAS fit is the integrated concentration along the light
150   path. As the light path depends on the measurement geometry, i.e. viewing angle, solar angle, and the radiative transfer, the

5

SCD is converted to the vertical column density (VCD, the vertically integrated concentration) via the so called air-mass-factor (AMF):

$$VCD = \frac{SCD}{AMF} \tag{2}$$

One simple approximation for the AMF is the geometrical AMF, depending only on the solar zenith angle (SZA) and viewing zenith angle (VZA):

$$AMF_{geo} = \frac{1}{SZA} + \frac{1}{VZA} \tag{3}$$

The geometric AMF is a valid approximation for stratospheric light paths in the UV if the SZA does not exceed $70°$ (Burrows et al., 2011) and accounts for the satellite and solar viewing geometry. For tropospheric columns, usually a more complex derivation using radiative transfer calculations is performed, including the trace gas profile (i. e. the plume height in the case of a volcanic plume), surface albedo and cloud cover. For trace gases close to the surface the AMF can be up to one order of magnitude lower compared to the geometric approximation (Theys et al., 2017).

In this study we employ only geometric AMFs, since (1) the focus of the study is to look at systematic influences and background corrections and (2) as the main focus of volcanic BrO is to derive the BrO/SO_2 ratio, for which the AMF divergence will cancel out in first approximation.

2.3 Selection of reference region

Traditionally, DOAS retrievals from satellites use the direct solar spectrum recorded on each day as a reference spectrum. This ensures that the DOAS retrieval can yield absolute slant columns of the respective trace gas. However, the direct solar spectra are obtained through a different optical input channel and traverses different optical parts (see Veefkind et al., 2012). Thus, these differences will cause stripes in the across-track direction (Richter and Wagner, 2001; Chance, 2007). While this can be corrected via so called »destriping« algorithm (e. g. Chance, 2007; Boersma et al., 2011; Hörmann et al., 2016), in recent times it has been found advantageous to use an earth-shine spectrum as reference spectrum for the retrieval (Theys et al., 2017; Seo et al., 2019). Ideally, such an earthshine spectrum is calculated from radiances obtained at regions where the respective trace gas is not abundant. Thus, regions over the equatorial Pacific are used (Sihler et al., 2012; Hörmann et al., 2013; Seo et al., 2019), far off potential anthropogenic pollution sources and remote from volcanoes. In this study, we expand the region an earth-shine spectrum is calculated using the complete equatorial latitude band as a reference region ($20°$ S to $20°$ N and $180°$ W to $180°$ E).

For SO_2, the assumption that remaining SO_2 is negligible holds true for this reference area. For BrO however, there is still a significant stratospheric background signal over the equatorial region with VCDs of roughly $3.5 \times 10^{13}\,\mathrm{molecules\,cm^{-2}}$, as stated by Richter et al. (2002) and also found within this study. Thus, using the earthshine reference will still yield differential SCDs instead of absolute SCDs. However, the stratospheric signal will introduce an offset in the resulting slant column densities, which is only slowly changing in spatial direction. In this study, the focus is on local volcanic plumes. Volcanic plumes
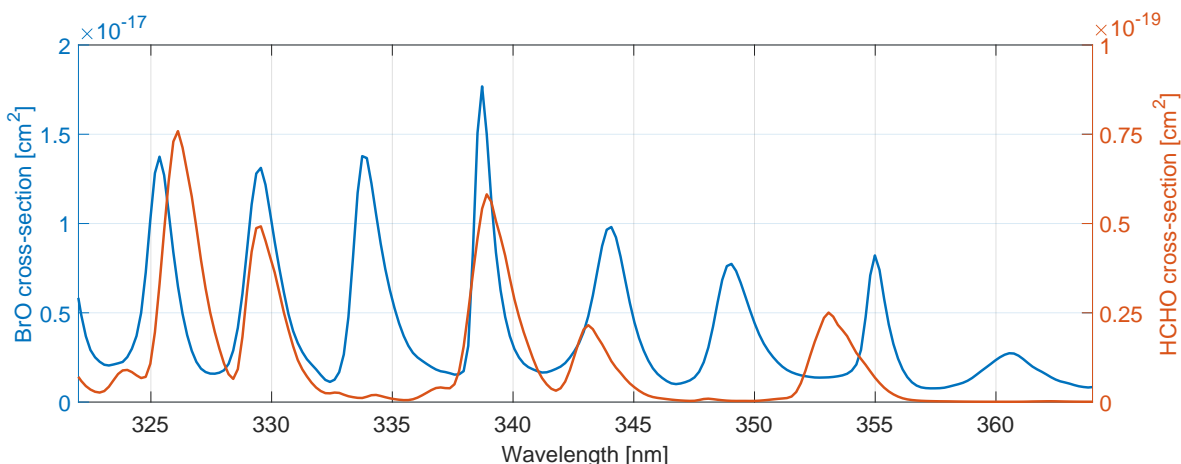
Figure 1. Absorption cross-section of BrO (blue) and HCHO (red) convolved with a typical TROPOMI instrument spectral response function.

are singular events, whose (1) spatial patterns usually have a high contrast compared to the background, and (2) spatial extent is almost always much smaller compared to stratospheric patterns. Thus, the stratospheric signal can be removed effectively by performing a local background correction for SO_2 and BrO (see Sect. 6.2).

185   The earthshine reference spectra are calculated in the following way: Firstly, all radiances within the global latitude band [$180°$ W to $180°$ E] around the equator [$20°$ S to $20°$ N] are selected, as mentioned above. In a second step, the radiances are normalized with respect to their maximum intensity in order to prevent that scenes or geometries which result in a brighter backscatter radiation, e.g. cloudy scenes, to be systematically weighted stronger. In the last step, the mean of the normalized radiances is taken as the daily reference spectrum in the DOAS analysis.

190   This process is performed separately for each spectra of the 450 across-track detector pixels of the TROPOMI instrument and for each day. A comparison of results using either an earthshine or a direct solar spectrum for measurements over the pacific region [$\pm20°$ N, $135 - 105°$ W] on 1 October 2018 is shown in Fig. 2. It can be seen that the retrieved VCDs show no difference (here the stratospheric influence in the irradiance data is eliminated for comparison by subtracting the mean BrO VCD). The fit root-mean-square (RMS), however, is about 25 % lower for the earthshine fit and roughly 6×10^{-3}. This RMS
195   distribution is in very good agreement with RMS reported over a similar pacific region by Seo et al. (2019) (cf. Fig. 11b) who employed a DOAS earthshine fit independently from the fit presented in this study.

3   Fit test setup

In the following sections, different wavelength ranges of the BrO DOAS fit are investigated. The performance with respect to the statistical variation, systematic spatial patterns of various origin and interference with HCHO is checked by comparing the
200   results of four fit wavelength ranges, where the upper fit range boundary is unchanged at $360\,\mathrm{nm}$, as varying the upper fit range
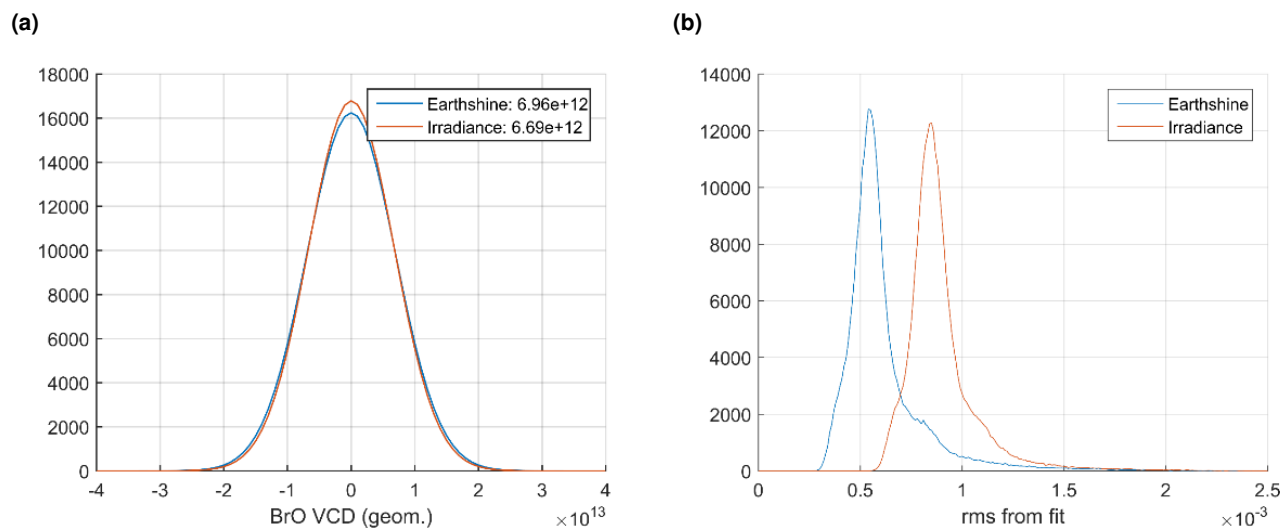
Figure 2. (a) Distribution of the BrO VCD and **(b)** the rms uncertainty of the DOAS fit for both, the irradiance and earthshine retrieval for the pacific region [±20°N, 135-105°W] on 1 October 2018. For the Irradiance BrO VCD the median BrO VCD (corresponding to the median stratospheric column) is subtracted in order for the two data-set to be comparable.

boundary was found to be less critical for the fit performance (Vogel et al., 2013; Seo et al., 2019). This upper wavelength fit range boundary is thus chosen at $360\,\mathrm{nm}$ as chosen in Sihler et al. (2012), which is used as a baseline BrO DOAS fit. The lower wavelength boundary is varied, yielding the following wavelength ranges:

– *336 - 360 nm*: This smallest fit wavelength range includes four BrO absorption bands (see Fig. 1) and is the baseline
205   wavelength range used by Sihler et al. (2012); Hörmann et al. (2013, 2016).

– *332 - 360 nm*: This fit wavelength range is chosen, because it adds one more BrO absorption band compared to the baseline, while adding no additional HCHO absorption band (see Fig. 1). This lower wavelength boundary is also used in Theys et al. (2011) (GOME-2) and Seo et al. (2019) (S-5P/TROPOMI). Theys et al. (2011) found that including this additional absorption band reduces the interference with HCHO.

210   – *323 - 360 nm*: This largest fit wavelength range was chosen, such that it includes seven BrO absorption bands while avoiding interference with very strong O_3 or SO_2 bands at wavelength below $320\,\mathrm{nm}$. It was not used in DOAS satellite retrievals so far due to the strong O_3 absorption for high latitudes.

– *323 - 328.5 & 332 - 360 nm*: This encompasses also the largest fit wavelength range, but the HCHO absorption band around $329\,\mathrm{nm}$, which overlaps with a BrO absorption band, is excluded in order to avoid HCHO interference (see
215   Fig. 1).

All four fit wavelength ranges are implemented with two different fit settings, which differ only in the inclusion and exclusion of the HCHO absorption cross section in the DOAS fit. Thus, there is a total set of eight different fits compared. The fits

including the HCHO absorption cross-section are labeled »HCHO«, the ones excluding HCHO are labeled »SR«(standard retrieval), i.e. the fit *HCHO 332 - 360 nm* corresponds to a DOAS fit evaluated in the wavelength range 332 nm to 360 nm

220 with the HCHO absorption cross-section included, while the fit labeled *SR 332 - 360 nm* corresponds to the same DOAS fit just without the HCHO absorption cross-sections included. These labels will be used throughout this paper. The overview over the DOAS fit settings, and the included absorption cross-sections for both *SR* and *HCHO* fits are listed in Table 1. Since the sensitivity study described in Sect. 4 suggests that the fit *SR 323 - 360 nm* is the most suitable fit (cf. Sect. 5), most of the results in the main part of the paper will be shown only for this fit. The corresponding results for the other fits can be found in the

225 appendix Sect. A1.

3.1 Overview of the fit performance

The global BrO VCD map for 1 October 2018 for the fit *SR 323 - 360 nm* is shown in Fig. 3. Enhanced BrO occurs at high latitudes and is caused by the stratospheric signal, related to variations in the tropopause height (Sihler et al., 2012; Schöne, 2023). Hence, the variations of the BrO dSCD is directly linked to variations in the ozone column, which in turn can be used

230 as a proxy for the strength of the stratospheric BrO column (Sihler et al., 2012). The enhanced BrO columns in southern high latitudes can be additionally caused by tropospheric BrO events occurring during polar spring (Sihler et al., 2012; Herrmann et al., 2022). In the equatorial region there are also distinct spatial patterns in the BrO columns not originating from volcanic plumes. They might be related to clouds and will be investigated in more detail in Sect. 4.1.

4 Investigation of systematic effects

235 In this section, the systematic influences of following three effects onto the BrO retrieval are investigated for the eight different BrO fit settings. Potential systematic influences of clouds and ozone in the polar as well as equatorial region onto the volcanic BrO data are described (Sect. 4.1) and corrected (Sect. 4.2). The question of spectral interference of HCHO is investigated and quantified (Sect. 4.3). Lastly, the overall effect of systematic influences is quantified (Sect. 4.4). Based on the latter as well as the statistical uncertainties (quantified in Sect. 5.1), an optimal fit setting is chosen in Sect. 5 and the combined fit uncertainty

240 is quantified for different volcanic scenarios globally.

4.1 Influence of clouds and ozone

The aforementioned structures in the global BrO map (cf. Fig. 3) are probably correlated to clouds (equatorial region) and the ozone column (high-latitude regions). To showcase this, we look at two regions: First, a pacific equatorial region ($[\pm 20°$ N, $160° - 100°$ W]), where the cloud structures are assumed to dominate the systematic structures, and second a high-latitude

245 region ($[40° - 60°$ N, $110° - 50°$ W]), where changes in the stratospheric column height are assumed to dominate the systematic structures in the BrO column. The former is depicted in Fig. 4 including both FRESCO CF (Fig. 4a) and FRESCO CH (Fig. 4c) as well as the BrO VCD for fit *SR 323 - 360 nm* (Fig. 4b). Furthermore, also the BrO VCD after applying the correction scheme for clouds and ozone (described in Sect. 4.2) is included in Fig. 4d.

Table 1. Fit settings for the eight BrO DOAS retrievals: Each wavelength fit range are applied once including and excluding the HCHO cross-section.

Wavelength fit ranges:	$323 - 360\,\text{nm}$
	$323 - 328.5\ \&\ 332 - 360\,\text{nm}$
	$332 - 360\,\text{nm}$
	$336 - 360\,\text{nm}$
Polynomial order:	5
Reference spectrum:	earthshine spectrum from equatorial region $[20^\circ\,\text{S} - 20^\circ\,\text{N};\ 180^\circ\,\text{W} - 180^\circ\,\text{E}]$ (cf. Sect. 2.3)
Absorption cross-section:	**Reference**
$O_3\,(223\,\text{K})$	Serdyuchenko et al. (2014)
$O_3\,(243\,\text{K})$	Serdyuchenko et al. (2014)
$SO_2\,(203\,\text{K})$	Bogumil et al. (2003)
$BrO\,(223\,\text{K})$	Fleischmann et al. (2004)
$O_4\,(203\,\text{K})$	Thalman and Volkamer (2013)
$OClO\,(293\,\text{K})$	Bogumil et al. (2003)
$NO_2\,(220\,\text{K})$	Vandaele et al. (1998)
$HCHO\,(298\,\text{K})^{\dagger}$	Meller and Moortgat (2000)
Pseudo absorber:	
Ring, norm	Wagner et al. (2009)
Ring, λ	Wagner et al. (2009)
Pukite, $O_3 \cdot \lambda$	Puķīte et al. (2010)
Pukite, $O_3{}^2$	Puķīte et al. (2010)
Shift & stretch	Beirle et al. (2013)
ISRF (w, aw, k)	Beirle et al. (2017)

†not included in SR fits.

It can be seen that the patterns in the BrO VCDs correlate to the cloud patterns and lower BrO VCDs are retrieved in the
250 presence of clouds. Furthermore, the impact of large cloud fractions and high cloud heights (e. g. around 15° N, 110° W) seems much stronger compared to large cloud fraction and low cloud height (e. g. arround -15° N, 110° W). This suggests that both cloud fraction (which is a measure for the fraction of a pixel area covered by a cloud) as well as the top height of clouds is influencing the spectroscopic response and cause a different BrO VCD response. Ideally, we would like to correct the cloud influence based on knowledge of its physical cause. However, it is unclear if this is simply due to shielding of the tropospheric
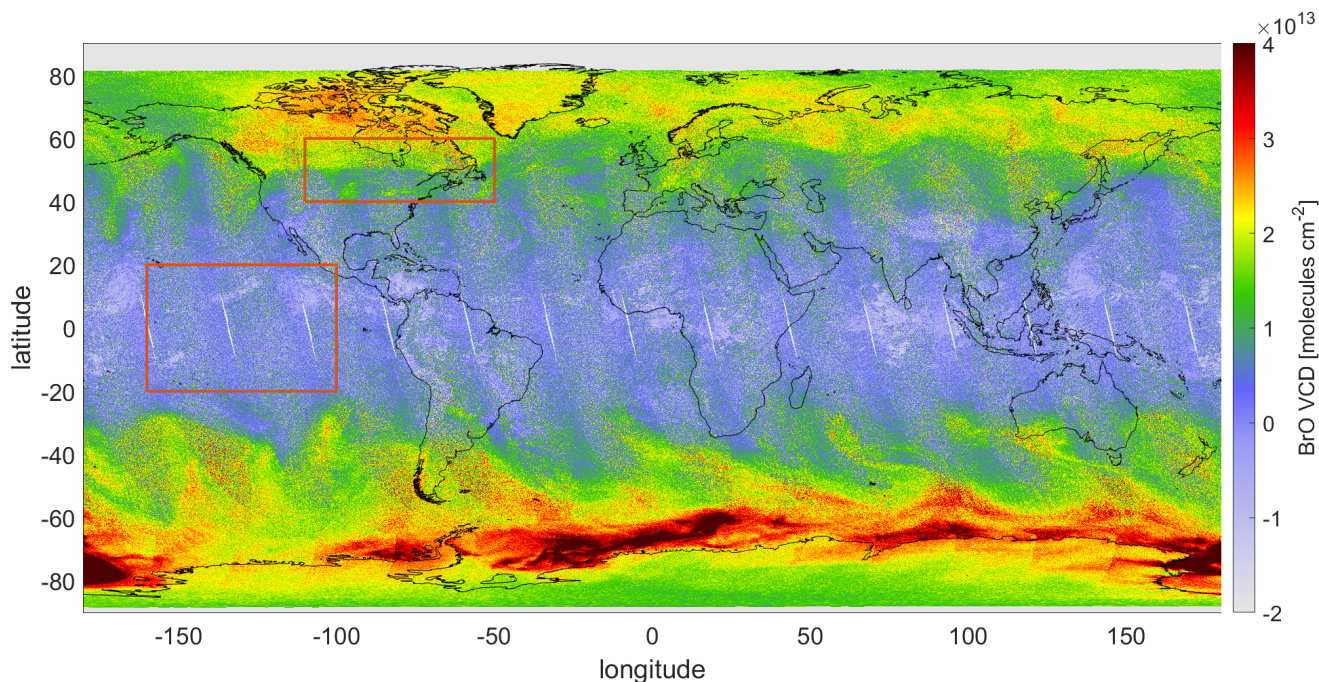
Figure 3. Global map of the BrO geometric VCD retrieved using the fit range *SR 323 - 360 nm* on 1 October 2018. The area of the cases shown in Fig. 4 and Fig. 5 are highlighted by the red squares.

255   BrO partial column below the clouds or a purely spectral response or has other origins. We therefore test a correction of these structures via an empirical scheme based on the two cloud parameters.

It is noteworthy that this decrease in the BrO column for cloudy scenes is an indication for cloud shielding of tropospheric BrO columns and can be used to derive and estimate for the tropospheric column, as done by Theys et al. (2011). However, as it is unclear if the cloud relation does not have a different origin and in this study we simply want to remove non-volcanic

260   influences on the BrO column, this question is not indulged further here.

The high-latitude example is depicted in Fig. 5, including the FRESCO CF (Fig. 5a) as well as the O_3 VCD (Fig. 5c) and the BrO VCD (Fig. 5b). There is a clear gradient in BrO VCD visible along $50°$ N, where BrO VCDs increase by more than $1 \times 10^{13} \, \mathrm{molecules \, cm^{-2}}$. This follows the gradient line of O_3 along the same latitude, indicating that this increase is most probably due to a higher stratospheric column. This gradient is overlayed by structures in the BrO VCD map south of $50°$ N,

265   e. g. between $40 - 45°$ N and $85 - 95°$ W. These coincide with cloud cover (indicated by the cloud fraction). In contrast to the equatorial region, the sign of the relation is inverted and high cloud fraction results in elevated BrO VCDs. Both these gradients and structures in the BrO VCD are reduced after applying the correction scheme (see Sect. 4.2), as can be seen in the corresponding map of the corrected BrO VCD (Fig. 5d).

In the following, we will investigate the cloud and ozone dependency for different latitudes. In order to investigate this

270   potentially systematic effect of clouds on the BrO retrieval, the individual pixels are sorted in bins of 0.05 cloud fraction
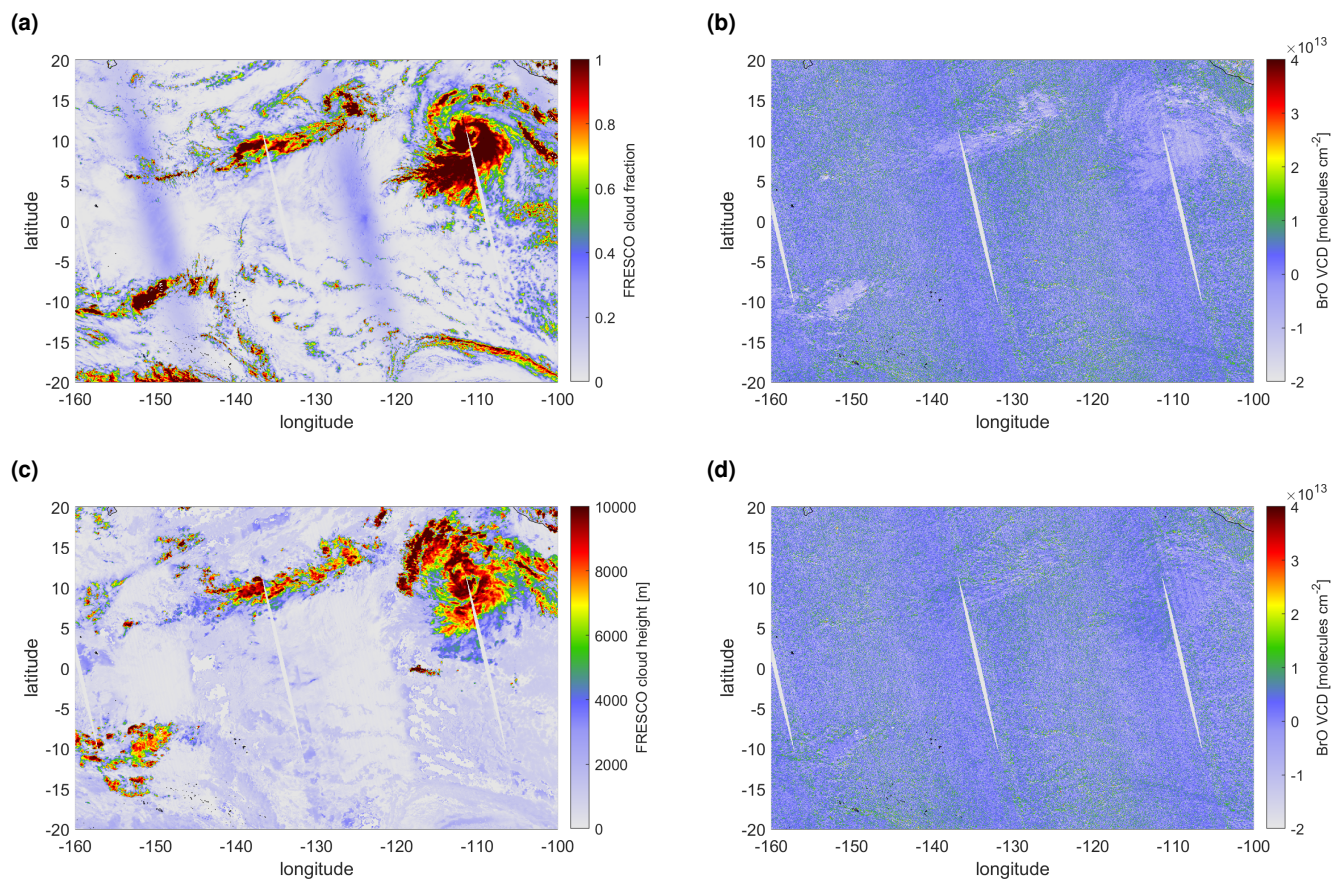
11

Figure 4. (a) FRESCO cloud fraction, **(b)** BrO VCD from fit *SR 323 - 360 nm*, **(c)** FRESCO cloud height, and **(d)** BrO VCD from fit *SR 323 - 360 nm* after applying the correction scheme. Data taken over the equatorial region $[\pm 20° N, 160° - 100° W]$ on 1 October 2018.

and $500\,\mathrm{m}$ cloud height (CH-CF bins). This is done first for the complete equatorial latitude band ($[\pm 20° N, \pm 180° E]$). The magnitude of the BrO response is quantified by taking the mean BrO VCD of all pixels in each respective bin.

The mean BrO VCD is systematically decreasing, both for increasing CH and increasing CF. The corresponding plots for all eight fits can be found in the appendix Fig. A1. The relation of the mean BrO VCD both to CH and CF appears to be almost
275 linear for all eight fit ranges, but with varying strength. Therefore this linearity seems independent of the fit settings chosen here allowing to derive a correction term, which will be described in Sect. 4.2.

While the cloud influence is very strong and rather linear for the equatorial region, there are also systematic structures in mid- and high latitudes (compare Fig. 3). Since these structures are not all related to the presence of clouds, but also to the O_3 columns (cf. Fig. 5) and possibly other factors, the same CH-CF binning is performed for $20°$ latitude bands over the whole
280 globe, which are shown in Fig. 6 for the fit *SR 323 - 360 nm*. The almost linear dependency on CH and CF observed for the
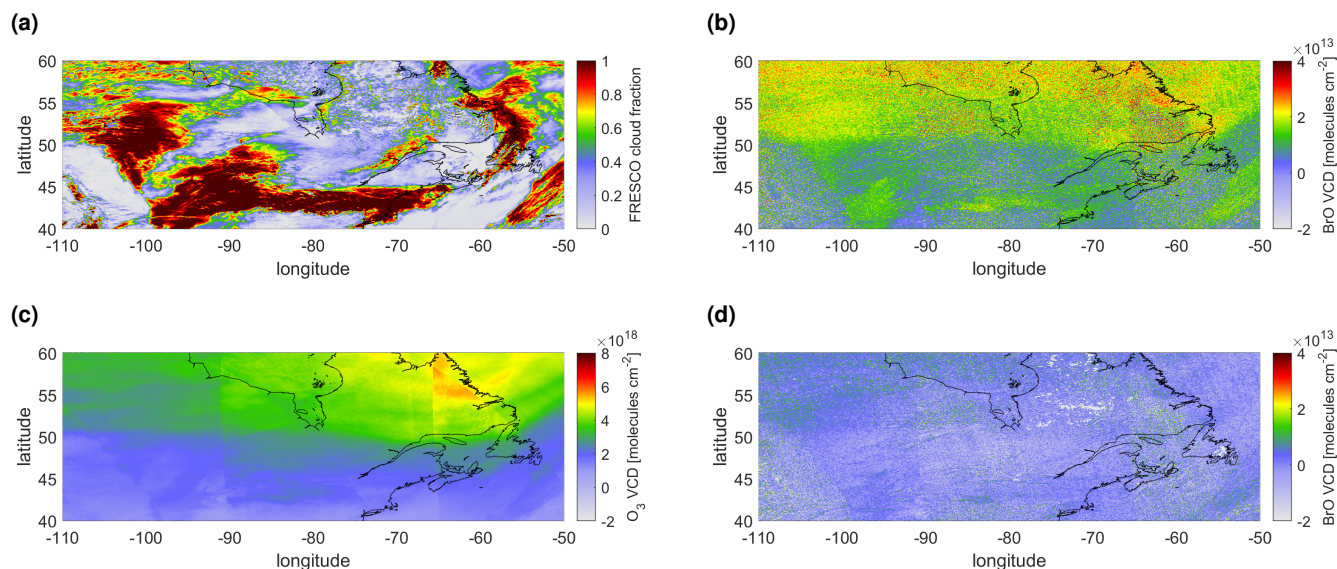
(a)

(b)

(c)

(d)

Figure 5. (a) FRESCO cloud fraction, **(b)** BrO VCD from fit *SR 323 - 360 nm*, **(c)** retrieved ozone VCD, and **(d)** BrO VCD from fit *SR 323 - 360 nm* after applying the correction scheme. Data taken over the northern high-latitude region [$40° - 60°$ N, $110° - 50°$ W] on 1 October 2018.

equator case is also found for neighbouring latitude bands from $30°$ S to $10°$ S and from $10°$ N to $30°$ N. For mid- to high latitudes north and south, this dependency of BrO on CH and CF is changing and/or is overlayed by other features.

While the general CH dependency of the BrO VCD (higher clouds, lower BrO VCD) is prevailing for high latitudes, the CF dependency is changing its sign, so that it is inverted for $70°$ N - $90°$ N, i. e. a lower cloud fraction leads to a lower BrO VCD. This is already observed in the case depicted in Fig. 5, indicating that this is a general finding applicable to high-latitudes and not specific to the case illustrated in Fig. 5. In addition, there is a positive BrO signal overlayed for cloud heights between 1000 and 5000 m, independent of cloud fraction. This dependency is clearly visible for northern latitudes ($30°$ N - $90°$ N), and appears to shift to higher cloud heights for higher latitudes, i. e. this shifts from $0 - 3000$ m, to $1000 - 4000$ m and to $2000 - 5000$ m CH for $30°$ N - $50°$ N, $50°$ N - $70°$ N, and $70°$ N - $90°$ N respectively. These structures in the CH-CF plot are most likely caused by an increase in the stratospheric slant column (due to the high SZA at high latitudes). For latitudes south of $50°$ S there are additional structures occurring, which are most likely attributed to tropospheric BrO enhancements during polar spring.

In order to correct for these systematic effects on the BrO VCDs, different correction approaches are investigated in the next section (Sect. 4.2). Since the dependency on cloud parameters is latitudinal dependent, the correction approach is applied to different latitude bands independently. Furthermore, since the systematic structures in high latitudes might be correlated to the stratospheric column, the inclusion of the O_3 VCD in the correction scheme as a first order indicator for the extent of the stratospheric column is tested.
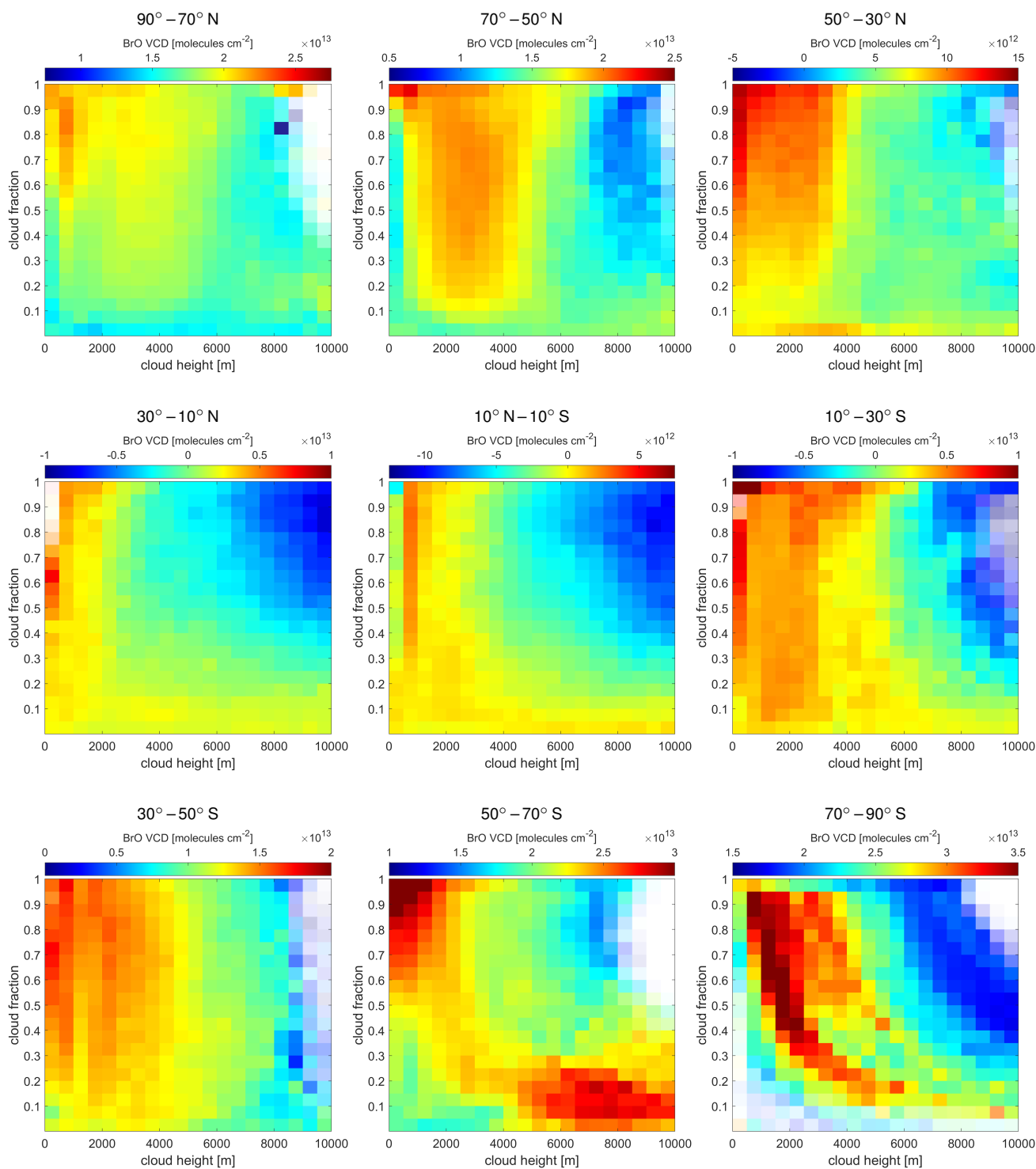
Figure 6. Mean BrO VCD for the cloud height - cloud fraction bins for the *SR 323 - 360 nm* fit for the global latitude bands in 20° steps from 90° N (upper left) to 90° S (lower right).

Table 2. Overview over the Cloud/O_3 correction schemes. The applied latitude region, the fitted parameter and their polynomial degrees are listed for the three correction schemes.

Name	latitude region	Fitted parameter	polynomial degree
ozone	70° S to 70° N	cloud height	2
		cloud fraction	2
		O_3 VCD	2
latitude	20° bands from 90° S to 90° N	cloud height	2
		cloud fraction	2
ozone latitude	20° bands from 90° S to 90° N	cloud height	2
		cloud fraction	2
		O_3 VCD	2

4.2 Cloud and ozone correction scheme

In order to investigate and correct the effects of the three parameters cloud fraction, cloud height, and O_3 VCD onto the BrO
300 VCDs, three multi-dimensional polynomial fitting schemes are tested on the BrO VCDs of 1 October 2018.

The three correction schemes are referred to as »ozone«, »latitude«, and »ozone latitude« in the following (see Table 2). All schemes include the two cloud parameters cloud fraction and cloud height derived from FRESCO. In addition, the schemes »ozone« and »ozone latitude« also include the O_3 VCD, taken from the BrO fit. Since there are two different O_3 absorption cross-sections (see below) as well as the two »Pukite«-pseudo absorbers included in the fit (see Table 1) to account for the
305 spectral absorption signal of O_3, the contributions of the individual fitted O_3 terms are combined to the complete slant column following Puķīte and Wagner (2016):

$$S_{O_3} = S_{O_3,223K} + S_{O_3,243K} + S_{O_3,\lambda}\lambda + S_{O_3,\sigma}\sigma_{O_3} \tag{4}$$

where the slant columns $S_{O_3,223K}$, and $S_{O_3,243K}$ correspond to the cross sections for two temperatures while the two last terms $S_{O_3,\lambda}$, $S_{O_3,\sigma}$ correspond to the two Pukite-term pseudo-absorbers (Puķīte et al., 2010), λ to the wavelength, and σ_{O_3}
310 to the ozone absorption cross-sections. For simplicity, the for the wavelength λ and the cross-section σ_{O_3} was taken only at the wavelength of the first maximum of the absorption cross section closest to the lower wavelength boundary (e. g. for the fit wavelength range $323--360$ nm: $\lambda = 325.0$ nm and $\sigma_{O_3} = 1.5 \times 10^{-20}$ cm^2 molecules^{-1}).

The resulting O_3 SCD S_{O_3} is then converted to the O_3 VCD via the geometric AMF. The O_3 VCD is then used in two of the three BrO correction schemes.

315   Each of the three BrO correction schemes is employed as a multi-dimensional polynomial P including the respective fitted parameters (see Table 2). The polynomial P comprising of p fitted parameters $x_1 \ldots x_p$ and their corresponding polynomial degrees $n_1 \ldots n_p$ is defined by in the following way:

$$P = \sum_{i_1=0}^{n_1} \cdots \sum_{i_p=0}^{n_p} c_{i_1,\ldots,i_p} \cdot x_1^{i_1} \ldots x_p^{i_p} \tag{5}$$

where $c_{i_1,\ldots,i_p}$ are the resulting fitted coefficients describing the dependency of the fitted quantity (in our case the BrO VCD) 320 to the fitting parameters (in our case cloud parameters).

    This means for example, that for the correction scheme »latitude« (see Table 2), where the fitted parameters are the cloud height and the cloud fraction with polynomial degree of two for both parameter, the polynomial P looks like:

$$P = \sum_{i,j=0}^{2} c_{i,j} \cdot [\mathrm{CH}]^i [\mathrm{CF}]^j \tag{6}$$

$$
\begin{aligned}
325 \quad P = \quad & c_{0,0} & & + c_{1,0} [\mathrm{CH}]^1 & & + c_{2,0} [\mathrm{CH}]^2 & \tag{7} \\
& + c_{0,1} [\mathrm{CF}]^1 & & + c_{1,1} [\mathrm{CH}]^1 [\mathrm{CF}]^1 & & + c_{2,1} [\mathrm{CH}]^2 [\mathrm{CF}]^1 & \tag{8} \\
& + c_{0,2} [\mathrm{CF}]^2 & & + c_{1,2} [\mathrm{CH}]^1 [\mathrm{CF}]^2 & & + c_{2,2} [\mathrm{CH}]^2 [\mathrm{CF}]^2 & \tag{9}
\end{aligned}
$$

    The principle output of this fit are the coefficients $c_{i_1,\ldots,i_p}$. Afterwards the polynomial P is subtracted from the uncorrected BrO VCDs forming the corrected BrO VCDs.

330   In this section the polynomial P is tested for the complete global data-set. However, for the the schemes »latitude« and »ozone latitude« there are separate sets of coefficients $c_{i_1,\ldots,i_p}$ for each $20°$ latitude band. Thus, for the retrieval of BrO inside a volcanic plume (Sect. 6) the correction coefficients can be calculated specifically for the latitude band around the volcano's latitude, ensuring a most accurate correction specific for each volcano's latitude.

    In the following, the correction schemes will be applied and discussed for the fit *SR 323 - 360 nm* only. The correction 335 schemes yield similar results for the other fits, but the fit *SR 323 - 360 nm* shows the best performance with respect to HCHO influence (see Sect. 4.3) and statistical uncertainties (see Sect. 5.1) and is therefore chosen as the best fit in the end.

    The corrected global maps – after applying the correction schemes »ozone«, »latitude« and »ozone latitude« – are schown in Fig. 7a-c respectively for the settings *SR 323 - 360 nm* (excluding HCHO). Note that the scale of the BrO VCD color-code differs from the uncorrected map (cf. Fig. 3).

340   The systematic structures in the equatorial region are effectively removed both by »latitude« and »ozone latitude« schemes (Fig. 7b,c). For the »ozone« correction scheme (Fig. 7a), however, the systematic structures prevail reduced in magnitude.

    The systematic structures in mid- to high-latitude are reduced for all three correction schemes. However, for the »latitude« scheme, which is the only one where the O_3 VCD is not included as a parameter, there are still significant structures visible for

latitudes larger than $30°$ N and S. The structures are best reduced by the »ozone latitude« scheme. However, it is important to note that even for this most sophisticated scheme, very strong BrO signals in the antarctic region uncorrelated with O_3 remain. These are probably tropospheric signals in the polar spring (compare Wagner and Platt, 1998; Sihler et al., 2012). If volcanic plumes are analysed for such conditions, the correction schemes developed in this study will not be able to separate the BrO in the volcanic plume form such events of enhanced tropospheric BrO.

For both, the »latitude« and the »ozone latitude« schemes, the correction is done separately for $20°$ latitude bands. It can be seen that on the edges of the latitude bands jumps in the BrO VCD are occurring (see Fig. 7b,c). However, for the »ozone latitude« scheme (Fig. 7c) these only occur at high latitudes. As the latitude band can be adjusted for each volcanic plume, they can be chosen so that the volcano is at the center of the latitude band so that the volcanic plume is not located on the edges. Furthermore, only a $20°$ latitude band around the volcano should be considered. Only very large plumes – recurring once every several years – might exceed this limit. For these cases the correction coefficient can also be applied For the development of a global BrO product including these corrections these jumps might be avoided by an interpolation of the correction parameter with latitude.

In order to quantify the efficacy of the different correction schemes, the mean of the corrected BrO VCD is calculated for each CH-CF bin for each latitude band independently. The corresponding plots are depicted in Fig. 8 for all three correction schemes as well as the bins without any correction. Ideally, there should be no or little dependency on the cloud parameters remaining after correction and no structures independent of the cloud parameter appearing.

All three correction schemes reduce the cloud dependency. It is noteworthy that the color-scale of the uncorrected plots is twice as large as the corrected ones.

It can be seen that the correction schemes working on each latitude band separately (»latitude« and »ozone latitude«) are much better at reducing the dependencies, both on cloud fraction as well as on cloud height compared to the global »ozone« scheme, which produces new CH-CF gradients in equatorial regions. However, these gradients are weaker than the original gradients.The »latitude« correction reduces most cloud dependencies for latitude bins between $90°$ N and $50°$ S. However, cloud independent signals remain in mid- to high-latitudes. The inclusion of ozone in the correction scheme (»ozone latitude«) is further reducing the cloud dependencies, but most importantly drastically reduces the cloud independent structures. For this scheme maximal differences in the CH-CF plots are typically $3 \times 10^{12}\,\mathrm{molecules\,cm^{-2}}$ for latitudes between $90°$ N to $50°$ S and $5 \times 10^{12}\,\mathrm{molecules\,cm^{-2}}$ for latitudes south of $50°$ S.

Thus, including ozone in the latitude dependent correction scheme (»ozone latitude«) appears to be the best correction both with respect to consistency in the global map (see Fig. 7c) and in the CH-CF bin plots (see Fig. 8). Therefore, this correction scheme is chosen for this study. In this approach the correction scheme is performed on separate $20°$ latitudinal bands. For the calculation of the correction factors, we thus propose to use the data on the $20°$ latitudinal band around the latitude of the volcanic plume.

From now on, all BrO VCDs used in this study will be by default corrected using the »ozone latitude« correction scheme.
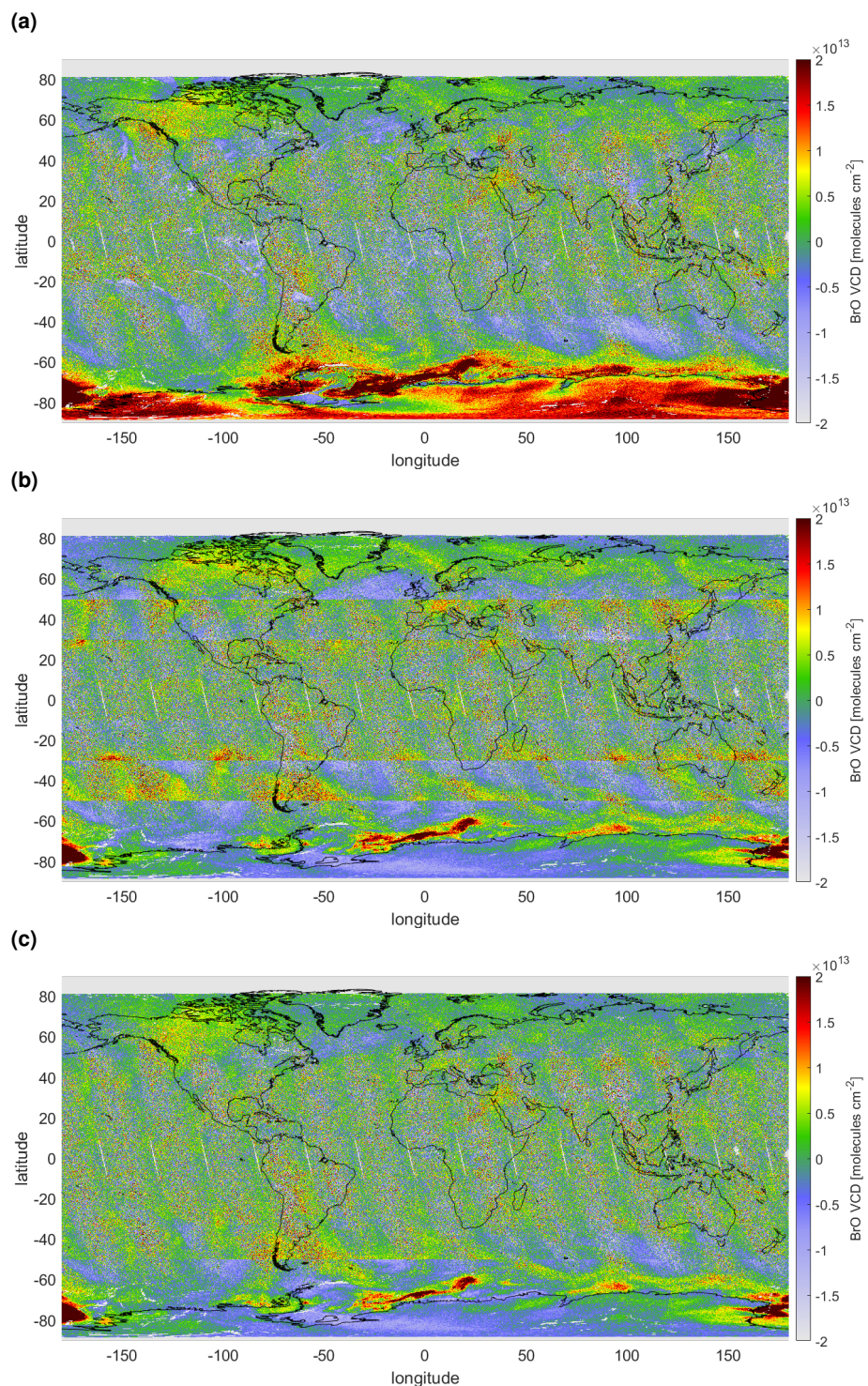
(a)

(b)

(c)

Figure 7. Global map of the BrO VCDs of the *SR 323 - 360 nm* fit **(a)** with ozone correction, **(b)** with CF and CH »latitude« correction only, and **(c)** CH, CF, and O_3 »ozone latitude« correction. The maps of the corresponding correction terms is plotted in Fig. A2.
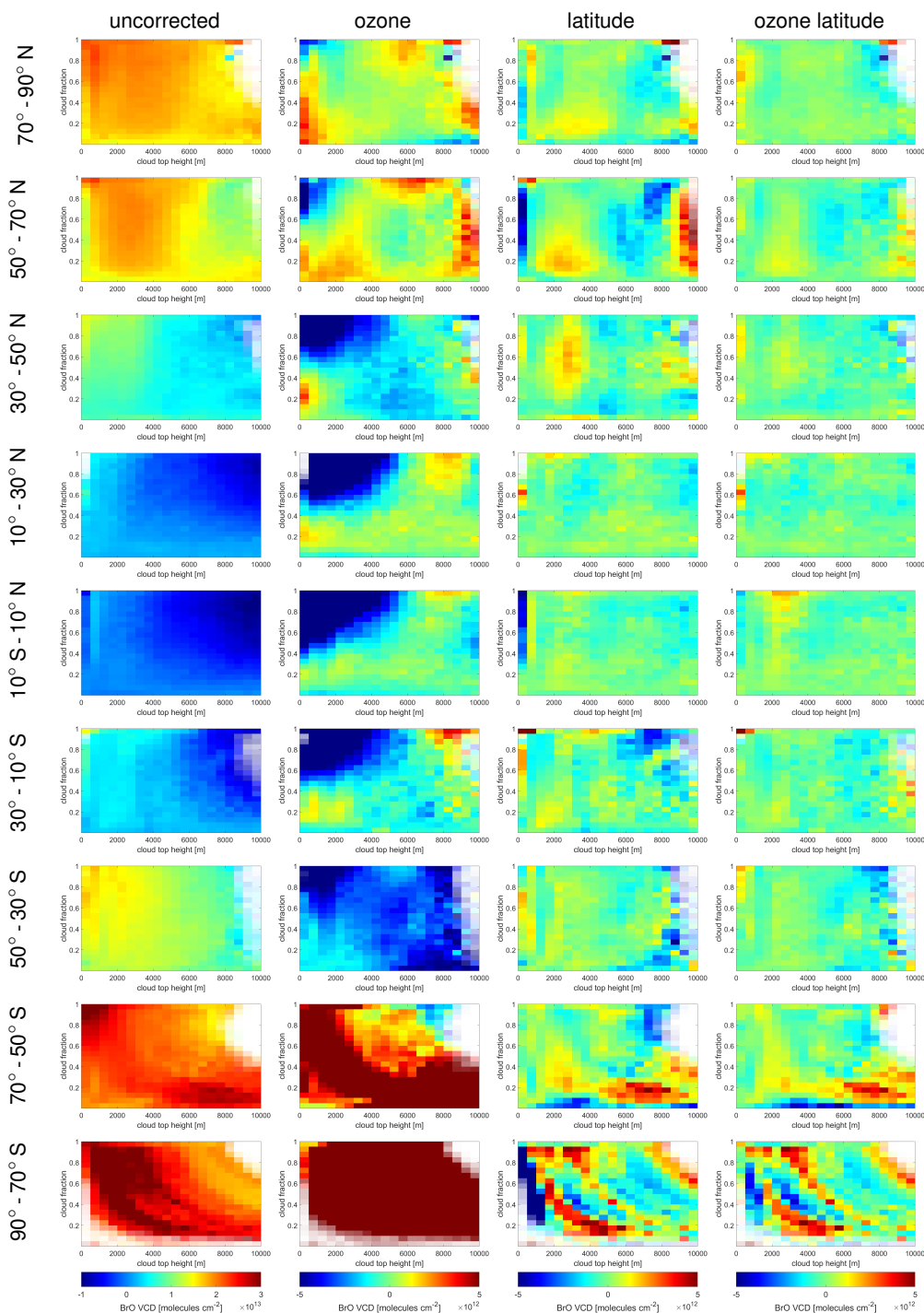
Figure 8. Mean BrO VCD as a function of the cloud height - cloud fraction bins for different latitude bands (rows from north to south) and correction schemes (from left to right): the uncorrected BrO VCD, and corrected BrO VCDs using ozone, latitude, and ozone latitude correction scheme. Note that the color scale range for the uncorrected plots is four times larger compared to the corrected plots.
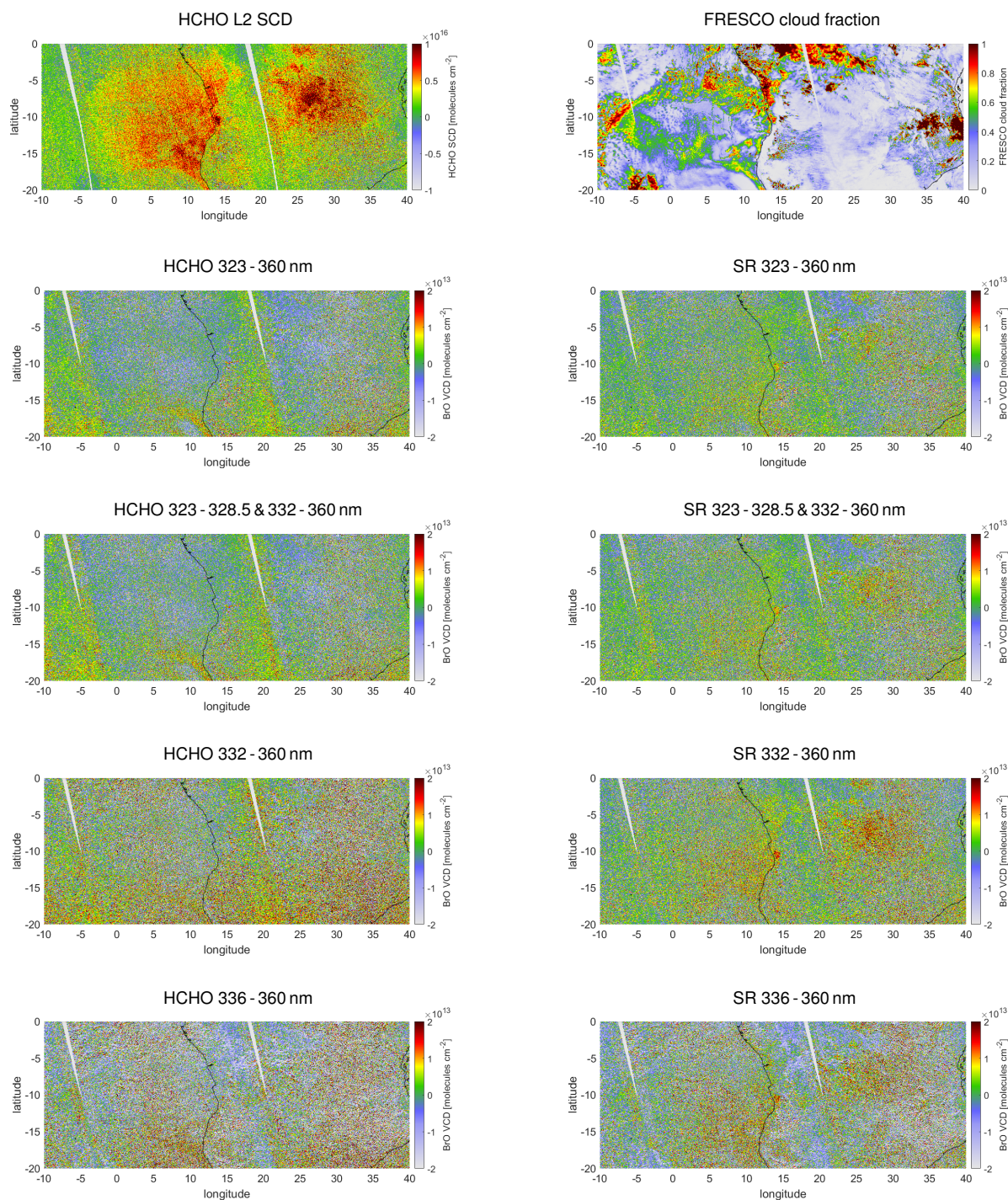
Figure 9. Maps of the auxiliary data and the BrO VCD for the eight fits over the African biomass burning region on 1 October 2018. *Topmost row, auxiliary data:* Operational S-5P/TROPOMI HCHO SCD (left) and FRESCO cloud fraction (right). *Below,* BrO *VCD:* BrO VCDs for the eight different fit ranges. The four fit wavelength ranges are listed from second top row to bottom row: *323 - 360 nm*, *323 - 328.5 & 332 - 360 nm*, *332 - 360 nm*, and *336 - 360 nm*. *Left column*: fits including HCHO (*HCHO*); *right column*: fits excluding HCHO (*SR*).

4.3 Influence of formaldehyde

Formaldehyde (HCHO) is an organic compound emitted into the atmosphere mostly via biogenic emissions or biomass burning. Highest columns are observed in tropical regions (De Smedt et al., 2018). Since the cross-sections of BrO and HCHO
380 in the UV range are very similar (see Fig. 1), atmospheric HCHO absorptions can cause systematic interference within the DOAS BrO retrieval.

This section is looking at the interference between HCHO and BrO for the eight BrO DOAS fits (defined in Sect. 3). The response of the different BrO fits to atmospheric HCHO absorption is investigated on the example of a biomass burning event in Africa between $0° - 20°$ S and $10°$ W $- 40°$ E on 1 October 2018.

385 The main questions is whether the inclusion of the HCHO absorption cross-section in the fit is necessary for the analysis of BrO in volcanic plumes, i. e. whether the exclusion of HCHO in the fit introduces a systematic offset in the BrO results in presence of enhanced HCHO absorption. One reason why it would be advantageous not to include the HCHO absorption cross-section is that the analysis yields a larger noise in the retrieved BrO SCDs if HCHO is included (as shown in Sect. 5.1). Equally important is the question, which fit wavelength range results in the lowest systematic influence of HCHO onto the
390 BrO results and to quantify the strength of a potential false BrO signal in the presence of enhanced HCHO absorption.

As information on the atmospheric HCHO column, the HCHO SCDs from the operational S-5P/TROPOMI HCHO L2 product (De Smedt et al., 2018) are used. The cloud information (cloud fraction and cloud height) is taken from FRESCO as in the previous sections.

The HCHO SCD derived from the operational S-5P/TROPOMI HCHO L2 product for the selected region is plotted in
395 Fig. 9 (noted »HCHO L2 SCD«, topmost left). There is a region of high HCHO columns exceeding $3 \times 10^{16} \, \mathrm{molecules \, cm^{-2}}$ on the African continent around $5°$ S and $29°$ E. Most importantly, this region is mostly cloud free (see Fig. 9, noted »FRESCO cloud fraction«, topmost right), ensuring minimal influence of clouds.

The BrO VCDs are corrected using the »ozone latitude« correction scheme described in Sect. 4.2. The corresponding maps for the eight fits are plotted in Fig. 9. The maps of the fits including HCHO (*HCHO*, Fig. 9 left column) do not reveal a distinct
400 positive BrO VCD signal in the region of the HCHO event. To the contrary, there rather seems to be a systematic negative offset in this region, most visible for the fits *HCHO 323 - 360 nm* and *HCHO 323 - 328.5 & 332 - 360 nm*. The fits excluding HCHO (*SR*, Fig. 9 right column), show a positive offset in the region of high HCHO SCDs. This is most prominent for the fit range *SR 332 - 360 nm* (fourth from top, right column), where the BrO VCDs exceed 1×10^{13} over a large area.

In order to investigate the potential systematic response of the BrO retrieval onto HCHO, the pixels are separated into bins
405 of HCHO SCD and cloud fraction. In order to separate the HCHO effect from potential cloud influence (which is also an error source in the operational HCHO fit, De Smedt et al., 2018), at this point only cloud free pixels are considered, i. e. cloud fractions below 0.1. The resulting mean BrO VCDs for the different HCHO bins for all eights fits are shown in Fig. 10. For the fits including the HCHO cross-section (*HCHO*, solid lines in Fig. 10) the BrO VCD is anti-correlated to the HCHO SCD, i. e. negative HCHO SCDs are found together with positive BrO SCDs which decrease almost linearly towards higher HCHO
410 SCDs. This is consistent for all four fit ranges. However, *HCHO 332 - 360 nm* and *HCHO 336 - 360 nm* shows the strongest

response, while the fits starting at $323\,\mathrm{nm}$ show a slightly weaker response. The fits not including the HCHO cross-section (*SR*, dashed lines in Fig. 10) show a positive response to HCHO, i. e. BrO SCDs increase for increasing HCHO SCDs. However, this only occurs for high HCHO SCDs and varies strongly for the different fit ranges. The effect is strongest for the fit range *SR 332 - 360 nm*, where BrO VCDs exceed $1 \times 10^{13}\,\mathrm{molecules\,cm^{-2}}$, whereas it is much less pronounced for the other fit ranges,

415   where maximal BrO VCDs are in the range of $5 \times 10^{12}\,\mathrm{molecules\,cm^{-2}}$. In addition, for low HCHO SCDs the BrO VCD changes only slightly or remains constant. This is most prominent for the fit range *SR 323 - 360 nm* (green dashed line). Here, the BrO VCDs are zero for HCHO SCDs below $1.5 \times 10^{16}\,\mathrm{molecules\,cm^{-2}}$. For higher HCHO SCDs, the BrO VCDs slowly increase, reaching about $5 \times 10^{12}\,\mathrm{molecules\,cm^{-2}}$ for maximal HCHO SCDs of about $4 \times 10^{16}\,\mathrm{molecules\,cm^{-2}}$. Interestingly the fit range *SR 323 - 328.5 & 332 - 360 nm*, in which an overlapping BrO/HCHO absorption band is left out compared to *SR*

420   *323 - 360 nm* and thus a weaker response would be expected, shows a higher false positive signal.

      In order to include also cloudy scenes, the mean BrO SCD is calculated for the complete HCHO-CF bins. The corresponding plots for the eight fits are shown in Fig. A3, where the four different fit wavelength ranges are plotted from left to right. The fits excluding the HCHO cross-section are in the upper row, while the fits including the HCHO cross-section are plotted in the lower row.

425   Both effects, the decreasing of BrO SCDs with increasing HCHO SCD for the fits including the HCHO cross-section (*HCHO*) as well as the opposite behavior of the fits not including the HCHO cross-section (*SR*), prevail also for cloudy scenes, but are sometimes weaker. Nevertheless, for volcanoes in regions where HCHO columns are high, it should be taken care for spatial HCHO patterns overlapping with the volcanic plumes (identified by its SO_2 signal).

      It can be thus concluded, that the inclusion of the HCHO cross-section in the BrO DOAS retrieval is not necessary. Even

430   though there can be a systematic false positive BrO response produced by very large HCHO columns, this effect is very low for the fit range *SR 323 - 360 nm*, with no response for HCHO SCDs below $1.5 \times 10^{16}\,\mathrm{molecules\,cm^{-2}}$ and a response not exceeding $5 \times 10^{13}\,\mathrm{molecules\,cm^{-2}}$ for very large columns. HCHO columns above $1.5 \times 10^{16}\,\mathrm{molecules\,cm^{-2}}$ are only observed for tropical biomass burning events, mostly ocurring around the equator, i. e. the systematic impact of HCHO on the BrO retrieval using the *SR 323 - 360 nm* fit is negligible for most cases.

435 **4.4   Quantifying the systematic effects**

In this section, the remaining potential systematic influence of clouds and other systematic effects onto the retrieval are investigated, i. e. the potential »false« BrO signal which could be created by clouds, ozone or other sytematic patterns. For this purpose the BrO VCD (after the correction with the »ozone latitude« correction scheme) is investigated for the fit *SR 323 - 360 nm*.

440   The uncertainties of any data-set is comprised of both statistical and systematic uncertainties. By averaging over neighbouring pixels the statistical variation can be gradually reduced and often the remaining uncertainties can be attributed to systematic effects. The statistical variation can be quantified by a Gaussian fit over the BrO distribution of the binned pixels. This Gaussian fit is performed separately for each latitude band as well as for each binning factor and the resulting standard deviations are plotted in Fig. 11.
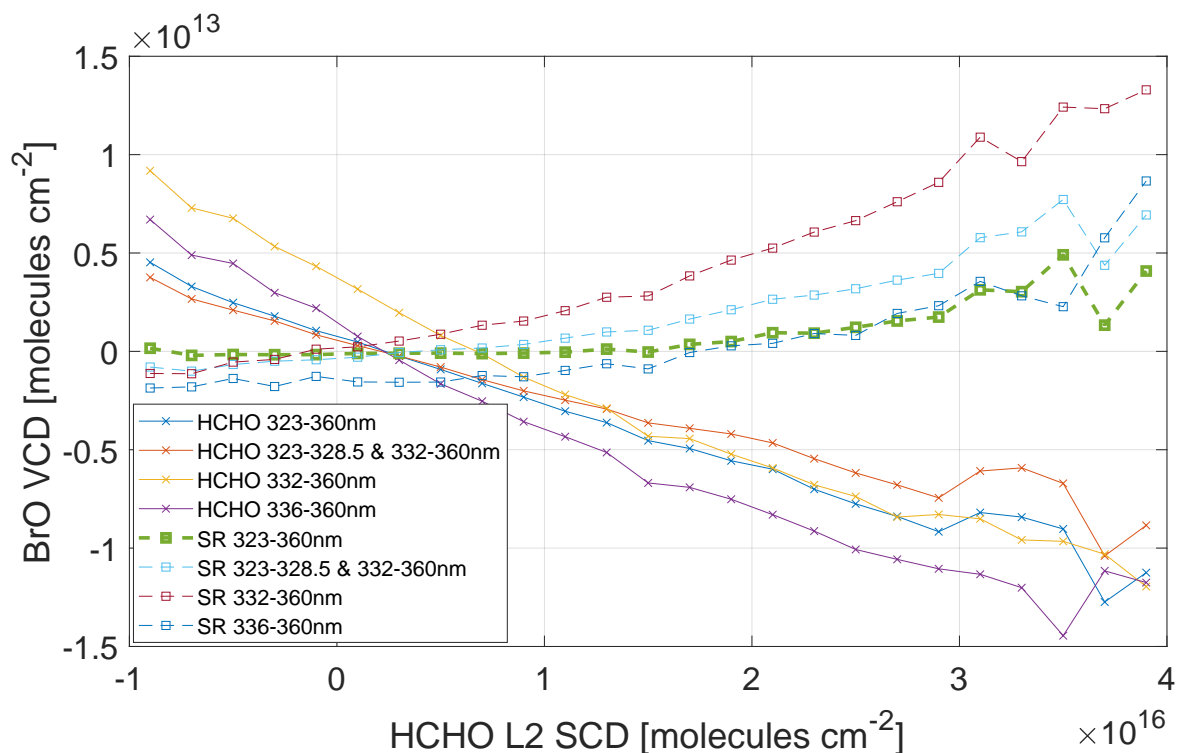
Figure 10. Mean BrO VCD as a function of HCHO SCD for the African biomass region on 1 October 2018 for the eight different fits including HCHO (*HCHO*) and excluding HCHO (*SR*). Only cloud free pixels (cloud fraction < 0.1) are considered.

445   It can be seen in Fig. 11 that the standard deviation is decreasing slower for increasing increasing binning factors (square root of the number of pixels binned) compared to the purely statistical model (black line in Fig. 11a) for all latitudes. For binning factors exceeding 20 (i. e. more than 400 pixels are binned together) the statistical model predicts a standard deviation of less than $5 \times 10^{11}\,\text{molecules cm}^{-2}$, while the measured data shows a standard deviation between 1 and $6 \times 10^{12}\,\text{molecules cm}^{-2}$ depending on the latitude. Thus, this remaining variance can be attributed to systematic effects. Around the equator ($10°$ S and

450    $10°$ N, Fig. 11b, violet square) the minimum standard deviation is almost $1 \times 10^{12}\,\text{molecules cm}^{-2}$, and this is chosen to be representative for the equator region. For the mid-latitudes below $50°$ latitude (triangles in Fig. 11), the bands on $10 - 30°$ N (green triangle), $30 - 50°$ N (light blue triangle), and $10 - 30°$ S (yellow triangle), the standard deviation is in the range of $1 - 1.5 \times 10^{12}\,\text{molecules cm}^{-2}$, while it is $2.5 \times 10^{12}\,\text{molecules cm}^{-2}$ for the band $30 - 50°$ S (light red triangle). We therefore choose the uncertainty to be $1.5 \times 10^{12}\,\text{molecules cm}^{-2}$ for mid-latitudes. For the high-latitudes north of $50°$ N (dark red

455   diamond and dark blue circle) and south of $50°$ S (blue diamond), there is a large difference. The northern high latitudes (dark red diamond and dark blue circle) show a standard deviation of $2.5 \times 10^{12}\,\text{molecules cm}^{-2}$ and $2.5 \times 10^{12}\,\text{molecules cm}^{-2}$, similar to the latitude band $30 - 50°$ S (light red triangle). The same latitude band in the south ($50 - 70°$ S, blue triangle), where the polar spring induces tropospheric BrO enhancements, which are not accounted for by the correction, yields a
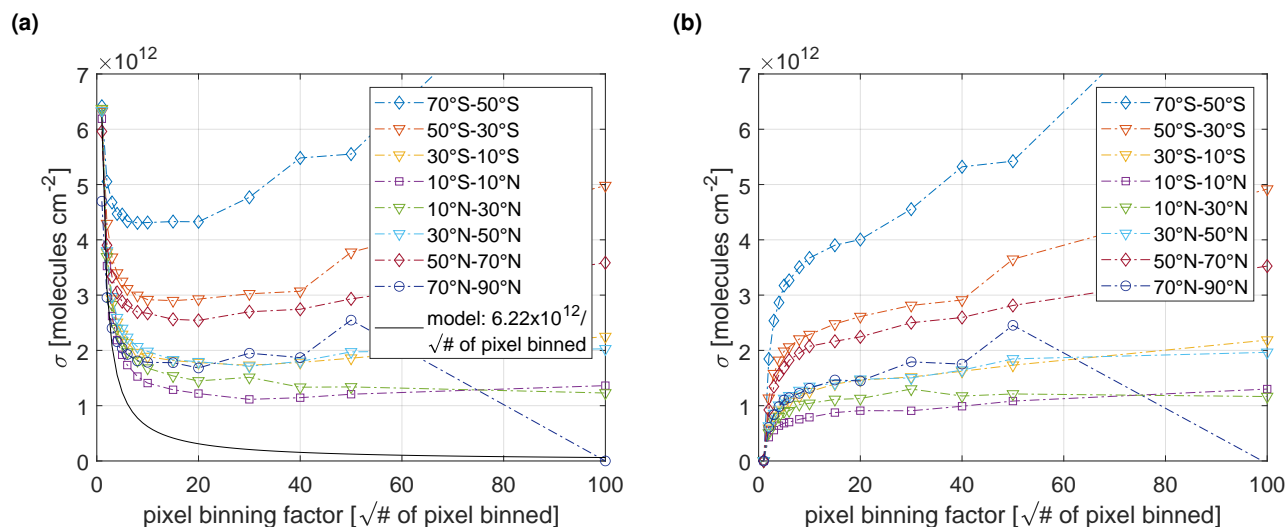
Figure 11. (a) The standard deviation of the BrO VCD distribution for different binnings for the seven latitude bands (colored lines). Also shown are the results of a model assuming that the total variation would be purely statistically distributed ($\frac{1}{\sqrt{N}}$, N=number of pixels binned, black line). **(b)** The difference to the statistical model is plotted for the seven latitude bands.

much higher standard deviation of 4.0×10^{12} molecules cm^{-2}. For high-latitudes, we therefore choose an uncertainty of $2.5 \times$ 10^{12} molecules cm^{-2} under normal conditions and an uncertainty of 4.0×10^{12} molecules cm^{-2} for polar spring conditions. The latitude band $70 - 90°$ S did not yield a meaningful gaussian fit due to the strong interference of enhanced tropospheric BrO event in polar spring. These uncertainties are then used as general systematic uncertainties in Table 4.

It is noteworthy that for high latitude bands of $70°$ S $- 50°$ S, $50°$ S $- 30°$ S and $50°$ S $- 70°$ N, there is even an increase in the standard deviation for binning factors above 20. This is due to the lower number of total pixel in this region. Due to the limited light availability in these regions (solar zenith angle $> 90°$), which will lead to an even smaller number of data-points after binning. This effect can be seen for all latitudes, where a slight increase in the standard deviation compared to lower binning factors is found.

5 Proposed fit settings for the retrieval of BrO in volcanic plumes

In addition to the systematic influences onto the BrO retrieval, the statistical uncertainties of the eight BrO DOAS fits also has to be taken into account in deciding which fit settings is optimal.

5.1 Quantifying the statistical uncertainties

In order to investigate the statistical performance of the BrO DOAS fit, the distribution of BrO VCDs in the equatorial region [$\pm 20°$ N, $180°$ W $- 180°$ E] is examined for all eight fit settings (see Fig. 12). The distributions are separated into the fits excluding the HCHO cross-section (*SR*, left), and the ones including the HCHO cross-section (*HCHO*, right), so that the same
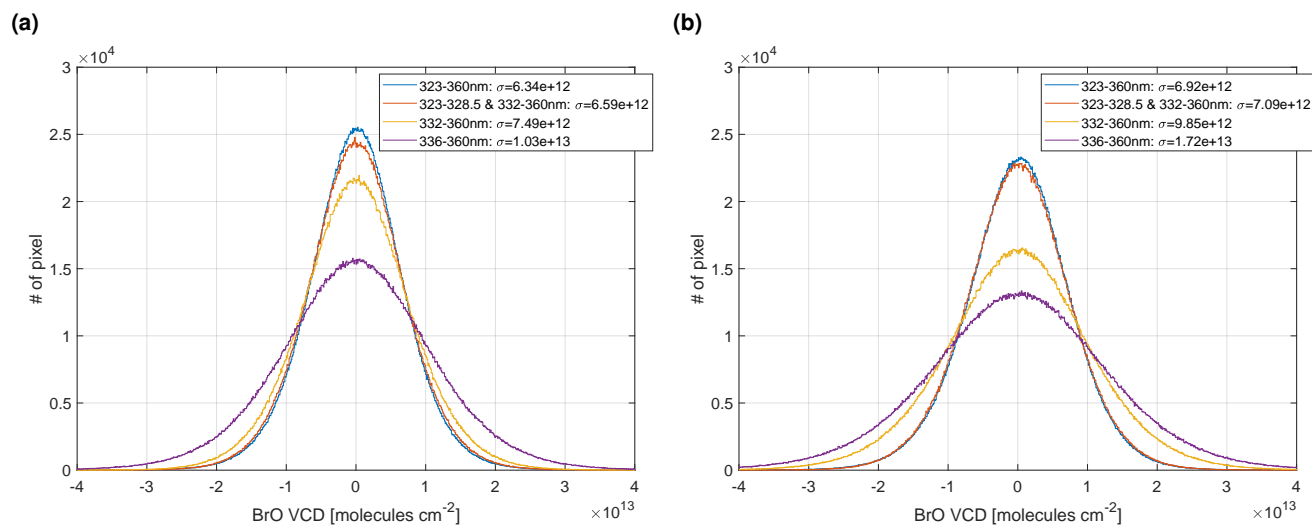
Figure 12. Distribution of BrO VCDs **(a)** for the four fits excluding HCHO (*SR*) and **(b)** including HCHO (*HCHO*). The corresponding standard deviations are given in the legend. All pixels on 1 October 2018 in the equator band between $20°$ S and $20°$ N over the whole longitude band are considered.

475 fit wavelength ranges have the same colors in both subplots. Increasing the fit wavelength range towards lower wavelength leads to a significant reduction in the statistical variation for both fit settings. For the *SR* fits the smallest fit range (*SR 336 - 360 nm*, which is the baseline fit range from Sihler et al. (2012)) shows a standard deviation σ of 1.03×10^{13} molecules cm^{-2}, which subsequently decreases to 7.49×10^{12} molecules cm^{-2} (*SR 332 - 360 nm*) and finally 6.34×10^{12} molecules cm^{-2} (*SR 323 - 360 nm*) when the wavelength range is expanded. This is to be expected as a larger wavelength range increases the information

480 content.

In comparison to the *SR* fits, the *HCHO* fits have a larger standard deviation for all wavelength ranges, leading to a minimal σ of 6.92×10^{12} molecules cm^{-2} (compared to 6.34×10^{12} molecules cm^{-2} for the corresponding *SR* fit) and a maximum σ of 1.71×10^{13} molecules cm^{-2} (compared to 1.03×10^{13} molecules cm^{-2} for the corresponding *SR* fit).

Thus, in order to achieve the lowest statistical uncertainties, the largest fit wavelength range excluding the HCHO cross-

485 section should be chosen (*SR 323 - 360 nm*).

Looking at the whole globe for the fit range *SR 323 - 360 nm* shows that the standard deviation is around 6.5×10^{12} molecules cm^{-2} for the mid-low latitude band between $70°$ S and $50°$ N (see Fig. 13a). In the arctic region, the standard deviation is gradually decreasing towards high northern latitudes, which can be due to the higher AMFs in high latitudes, i. e. the variation of the SCD is divided by a larger number. In the Antarctic region, the standard deviation also decreases for a latitude of $80°$ S. However,

490 the distribution is not well represented by a gaussian distribution (see Fig. 13b, blue lines). There is a positive tail of elevated BrO VCDs due to enhanced tropospheric BrO columns in polar spring events. Furthermore, the distribution is not centered around zero, i. e. the correction term is offset.
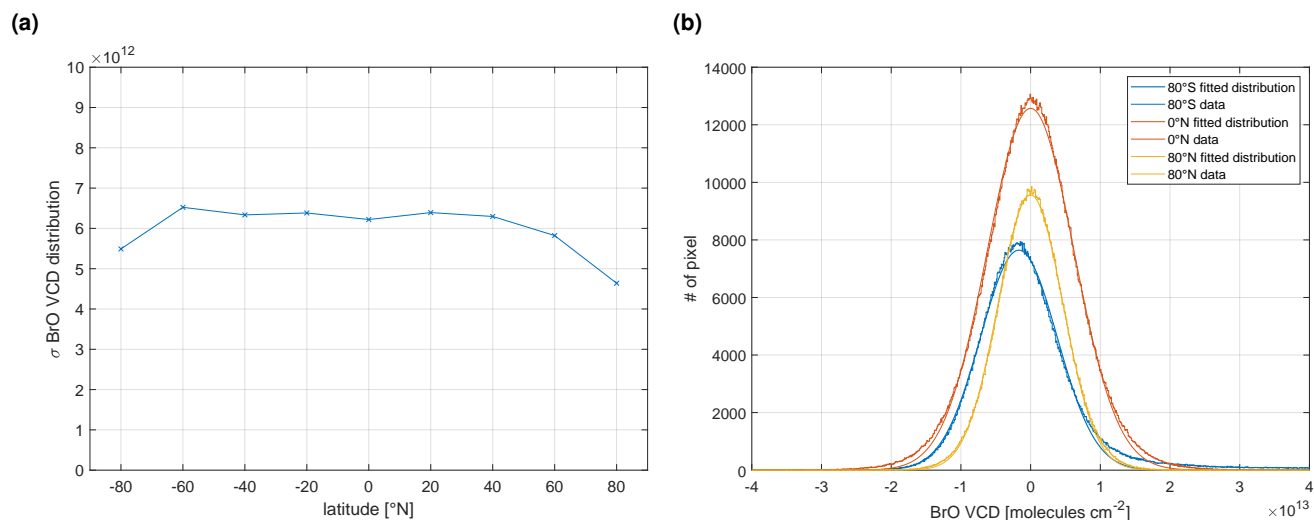
25

(a)

(b)

Figure 13. Latitudinal variation of the statistical uncertainty. **(a)** Standard deviation σ of the distribution of the BrO VCD of fit *SR 323 - 360 nm* for different latitude bands on 1 October 2018. **(b)** BrO VCD distribution of fit *SR 323 - 360 nm* for $80°$ S (blue), $0°$ S (red), and $80°$ N (yellow). The corresponding fitted gaussian distributions are indicated by a solid line in the respective color.

Concluding, the statistical variation of the fit *SR 323 - 360 nm* can be best estimated by the standard deviation of 6.5×10^{12} molecules cm^{-2} or less for all latitudes.

5.2 Summary of the findings

The investigation of the eight different fits can be summarized by the following:

- The statistical uncertainty decreases if (1) the wavelength fit range of the fit is increased and (2) the HCHO cross section is not included in the DOAS fit.

- The systematic influence of clouds and the stratospheric background can be well corrected by the correction scheme described in Sect. 4.1 for all eight fits. Thus, there is no preference for a fit range or fit setting.

- The influence of HCHO is lowest for the fit *SR 323 - 360 nm*. The BrO column shows no cross-sensitivity for moderate HCHO columns and the lowest increase for very high HCHO columns.

Thus, the fit range *SR 323 - 360 nm* is chosen for the BrO DOAS evaluation, since it shows the lowest statistical variation and is least susceptible to HCHO interference. The complete overview of the DOAS fit settings for this fit is listed in Table 3. The chosen best fit settings are recommended also for further studies on BrO in volcanic plumes.

Table 3. Fit settings for the selected BrO DOAS retrieval.

Wavelength range:		$323 - 360\,\mathrm{nm}$
Polynomial order:		5
Reference spectrum:		daily earthshine spectrum from equatorial region [$20°\,\mathrm{S} - 20°\,\mathrm{N}$; $180°\,\mathrm{W} -$ $180°\,\mathrm{E}$] (see Sect. 2.3)

Absorption cross-sections:

Species	Temperature	Reference
O_3	$223\,\mathrm{K}$	Serdyuchenko et al. (2014)
O_3	$243\,\mathrm{K}$	Serdyuchenko et al. (2014)
SO_2	$203\,\mathrm{K}$	Bogumil et al. (2003)
BrO	$223\,\mathrm{K}$	Fleischmann et al. (2004)
O_4	$203\,\mathrm{K}$	Thalman and Volkamer (2013)
OClO	$293\,\mathrm{K}$	Bogumil et al. (2003)
NO_2	$220\,\mathrm{K}$	Vandaele et al. (1998)

Pseudo absorber:

Ring, norm	$230\,\mathrm{K}$	Wagner et al. (2009)
Ring, λ	$230\,\mathrm{K}$	Wagner et al. (2009)
Pukite, $O_3 \cdot \lambda$	$223\,\mathrm{K}$	Puķīte et al. (2010)
Pukite, $O_3{}^2$	$223\,\mathrm{K}$	Puķīte et al. (2010)
ISRF	w, aw, k	Beirle et al. (2017)
Shift & stretch		Beirle et al. (2013)

5.3 Estimation of the combined statistical and systematic uncertainties

In this section, the error estimations from the previous sections are summarised for all different cases identified throughout these sections and the total error is calculated. Three latitude regions are selected: Equator is the latitude band between $20°\,\mathrm{S}$ and $20°\,\mathrm{N}$, mid-latitudes stretch from the equatorial region to $50°\,\mathrm{N}$ and $50°\,\mathrm{S}$, and high latitudes are further north/south. In addition, there are two special cases distinguished: The polar spring in high latitudes with increased tropospheric BrO columns and biomass burning events which are typically located close to the equator. Since biomass burning can seldomly also occur in mid-latitude or boreal summer, these cases are included as well.

Finally, for each of these cases the statistical uncertainty and the systematic uncertainties are added quadratically:

$$\sigma_{combined} = \sqrt{\left(\sum \sigma_{systematic}\right)^2 + \left(\sigma_{statistical}\right)^2} \tag{10}$$

27

515   The systematic uncertainties comprise those derived in Sect. 4.4 for each latitude region and the systematic uncertainties caused by large HCHO columns, derived in Sect. 4.3 (depicted in Fig. 10). The statistical uncertainties are derived for each latitude region in Sect. 5.1 (depicted in Fig. 13).

The added systematic, statistical, and the combined overall uncertainties are shown for all cases in Table 4. Under normal conditions (that means in the absence of high HCHO columns and polar tropospheric BrO enhancements), the combined

520   uncertainty is between 6.6 and $7.0 \times 10^{12} \, \mathrm{molecules \, cm^{-2}}$. Such conditions are representative for most of the volcanoes, e. g. the island volcanoes in the equatorial region (Galapagos, Vanuatu, Mayon) but also all mid- as well as high-latitude volcanoes such as Etna, Kilauea, and La Palma as well as Kamchatka, Iceland and the Aleutian volcanic regions.

The volcanoes with a risk of a general influence of biomass burning are located in the equator region in the vicinity of rain forest. These are most notably the African rift valley volcanoes Nyiragongo/Nyamuragira, the northern Andes volca-

525   noes – e. g. Nevado del Ruiz – and the Central American volcanic Arc volcanoes – e. g. Masaya and Fuego. Here, an uncertainty of $7.4 \times 10^{12} \, \mathrm{molecules \, cm^{-2}}$ has to be assumed. While mid- to high-latitude volcanic regions can also be affected by high HCHO columns which would increase the combined uncertainty by roughly $0.8 \times 10^{12} \, \mathrm{molecules \, cm^{-2}}$ to 7.6 to $8.2 \times 10^{12} \, \mathrm{molecules \, cm^{-2}}$, this is expected only under very rare circumstances.

6   Retrieval of BrO inside volcanic plumes

530   This section shows the final selected retrieval of BrO inside volcanic plumes. The SO_2 DOAS retrieval is quickly explained (cf. Sect. 6.1) as well as the additional local background correction (cf. Sect. 6.2). The retrieval steps are: The proposed BrO DOAS fit in the chosen wavelength range of $323 - 360 \, \mathrm{nm}$ (cf. Sect. 5) is performed and the latitudinal background correction (cf. 4.2) is applied. The plume is masked based on the SO_2 signal, whose retrieval is explained in Sect. 6.1. This mask is used for a secondary local background correction (cf.Sect. 6.2). The results of all the different steps is discussed in detail in Sect. 6.3.

6.1 SO_2 retrieval

SO_2 is one major constituent of volcanic gas plumes, accounting for $1 - 25 \, \%$ of the volcanic gas emissions (Textor et al., 2004). In contrast to BrO, there is no significant stratospheric column of SO_2. As SO_2 has also differential absorption structures in the UV, it is widely used as a indicator for the detection of volcanic plumes (e. g. Hörmann et al., 2013; Fioletov et al., 2016; Carn et al., 2017).

540   DOAS SO_2 retrievals from satellites were performed starting with the launch of the Global Ozone Monitoring Experiment (GOME) in 1995 (Eisinger and Burrows, 1998; Thomas et al., 2005; Khokhar et al., 2005); later DOAS retrievals were implemented also for the SCanning Imaging Absorption SpectroMeter for Atmospheric CHartographY (SCIAMACHY) (Afe et al., 2004), GOME-2 (Rix et al., 2012; Hörmann et al., 2013), the Ozone Monitoring Instrument (OMI) (Theys et al., 2015) and most recently for TROPOMI (Theys et al., 2017). As SO_2 columns in volcanic plumes vary over multiple orders of magnitude,

545   recent algorithms introduced a scheme using multiple fits in different wavelength ranges with varying SO_2 absorption strength (Hörmann et al., 2013; Theys et al., 2015; Warnach, 2022).

Table 4. Overview of the different systematic influence contributions.

Error class	systematic		statistical	combined	affected volcano/
Error origin	general	HCHO			volcanic region
molecules cm^{-2}	$\times 10^{12}$	$\times 10^{12}$	$\times 10^{12}$	$\times 10^{12}$	
Equator:					
normal	1.0	–	6.5	6.6	Vanuatu islands
					New Zealand
					Galapagos islands, Ecuador
					Piton de la Fournaise, France
					Anak Krakatau, Indonesia
biomass burning	1.0	2.5	6.5	7.4	DR Congo
					Central American Volcanic Arc
					Central American Volcanic Arc
					South East Asian volcanoes
Mid-latitudes:					
normal	1.5	–	6.5	6.7	Italian volcanoes
					Canaries, Spain
					Azores, Portugal
					Hawaii, USA
					Mainland USA
					Chile and Peru
					Japan
biomass burning	1.5	2.5	6.5	7.6	–
High-latitudes:					
normal	2.5	–	6.5	7.0	Aleutian islands[†], USA
					Kamtchatka, Russia
					Iceland volcanoes
polar spring	4.0	–	6.5	7.6	Mt. Erebus, Antarctica
biomass burning	2.5	2.5	6.5	8.2	–

In this study, an SO_2 retrieval is employed purely to identify the volcanic plume for an accurate local background correction of BrO (see next section). Thus, only the fit range of $312 - 324\,nm$, already sensitive to small SO_2 columns, is employed. This fit range is used in the SO_2 verification algorithm for TROPOMI (developed by C. Hörmann, MPIC, Mainz), and refined by S. Warnach, MPIC, within the verification for the upcoming Sentinel-5 mission (van Roozendael and the Sentinel 5 Verification team) as well as on synthetic spectra within the SO_2 verification for the upcoming Sentinel-4 mission (Wagner and the Sentinel 4 Verification team). In all these verification exercises very good agreement was found to the operational algorithm of S-5P/TROPOMI (Theys et al., 2017).

The DOAS fit settings for the SO_2 retrieval includes the SO_2 absorption cross-section ($203\,K$, Bogumil et al., 2003), and two O_3 absorption cross-sections (223 & $243\,K$, Serdyuchenko et al., 2014). The other fit parameters (pseudo-absorbers), and the Fraunhofer reference are identical to those of the BrO fit. A detailed description of the SO_2 retrieval can be found in Warnach (2022).

6.2 Local background correction

In order to correct for a potential remaining spatial pattern in the background distribution of SO_2 as well as BrO, a spatial polynomial correction is applied. This spatial polynomial was already successfully implemented as a local background correction in Hörmann (2013). Even though the BrO and SO_2 retrieval and correction schemes presented in this study are much less affected by background gradients due to the inclusion of Pukite-Terms for O_3 and the aforementioned cloud-ozone correction scheme, there are still potential small spatial patterns remaining, which should be further reduced.

The retrieved VCD V_m can be decomposed into the background VCD V_b and the volcanic VCD V_v:

$$V_m = V_b + V_v \tag{11}$$

The spatial polynomial correction scheme makes use of the fact that volcanic plumes can usually be considered as a localized phenomenon of several $100\,km$ extent within a large scale background distribution pattern on the scale of $1000\,km$ for both BrO and SO_2. Furthermore, both volcanic and background distributions are independent from each other and it can be assumed that the background is smooth with respect to the scale of the volcanic plume and background information gathered spatially around the plume can be interpolated over the plume region.

The background VCD V_b for each pixel k is modeled by two-dimensional polynomial of degree three:

$$[V_b]_k = \sum_{i,j=0}^{3} c_{i,j} \cdot x_k^i \cdot y_k^j \tag{12}$$

where x is the pixel latitude and y the longitude corrected by a latitudinal dependent squeeze:

$$[V_b]_k = \sum_{i,j=0}^{3} c_{i,j} \cdot [\text{lat}]_k^i \cdot [\text{lon} \cdot \cos(\text{lat})]_k^j \tag{13}$$
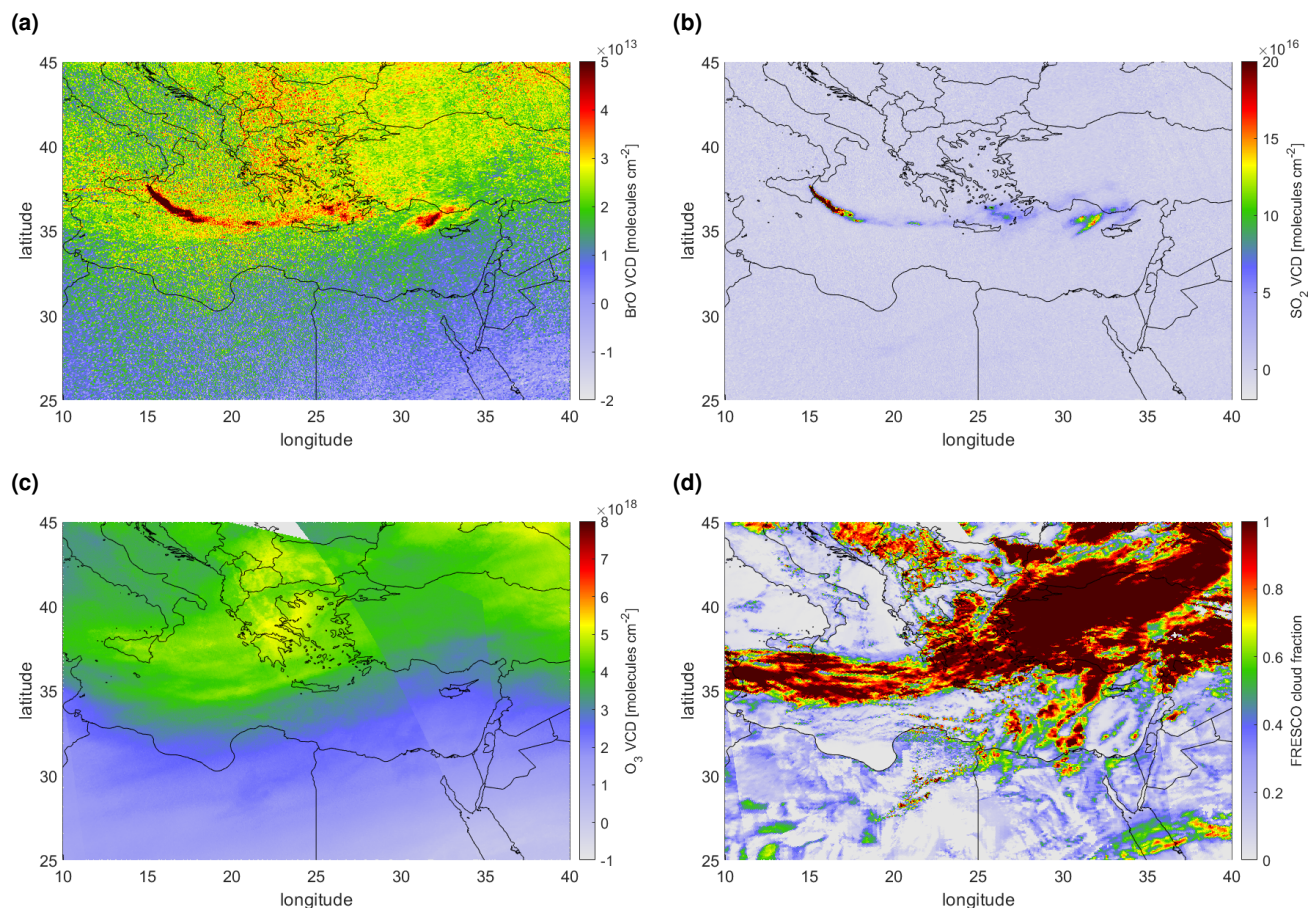
(a)

(b)

(c)

(d)

Figure 14. Plume of Mt. Etna on 25 December 2018. **(a)** The BrO VCD map and **(b)** the SO_2 VCD map without correction. **(c)** The O_3 VCD derived from the BrO fit and **(d)** the cloud fraction (from FRESCO), both used in the lat ozone correction scheme.

575   In order to calculate the polynomial, first the volcanic plume is masked. For this a SO_2 VCD threshold is chosen, above which a pixel is masked as influenced by the volcanic plume. This is chosen in this study as four times the standard deviation of SO_2 (for TROPOMI typically in the range of $2 \times 10^{16}\,\mathrm{molecules\,cm^{-2}}$, compare Warnach, 2022). The polynomial coefficients $c_{i,j}$ are then determined for this subset of data for both BrO and SO_2 independently and applied to each pixel of the complete data-set, leading to the background VCD. The resulting (volcanic) VCD is obtained by subtracting the background VCD V_b

580   from the retrieved VCD V_m.

6.3   Results

The complete sequence of processing steps of the retrieval of BrO for a volcanic plume is shown for the example of the plume of Mt. Etna, Italy, on 25 December 2018. The BrO and SO_2 VCD maps derived from the respective DOAS retrievals as well as the calculated O_3 VCD and the FRESCO cloud fraction are depicted in Fig. 14a-d respectively. The volcanic plume
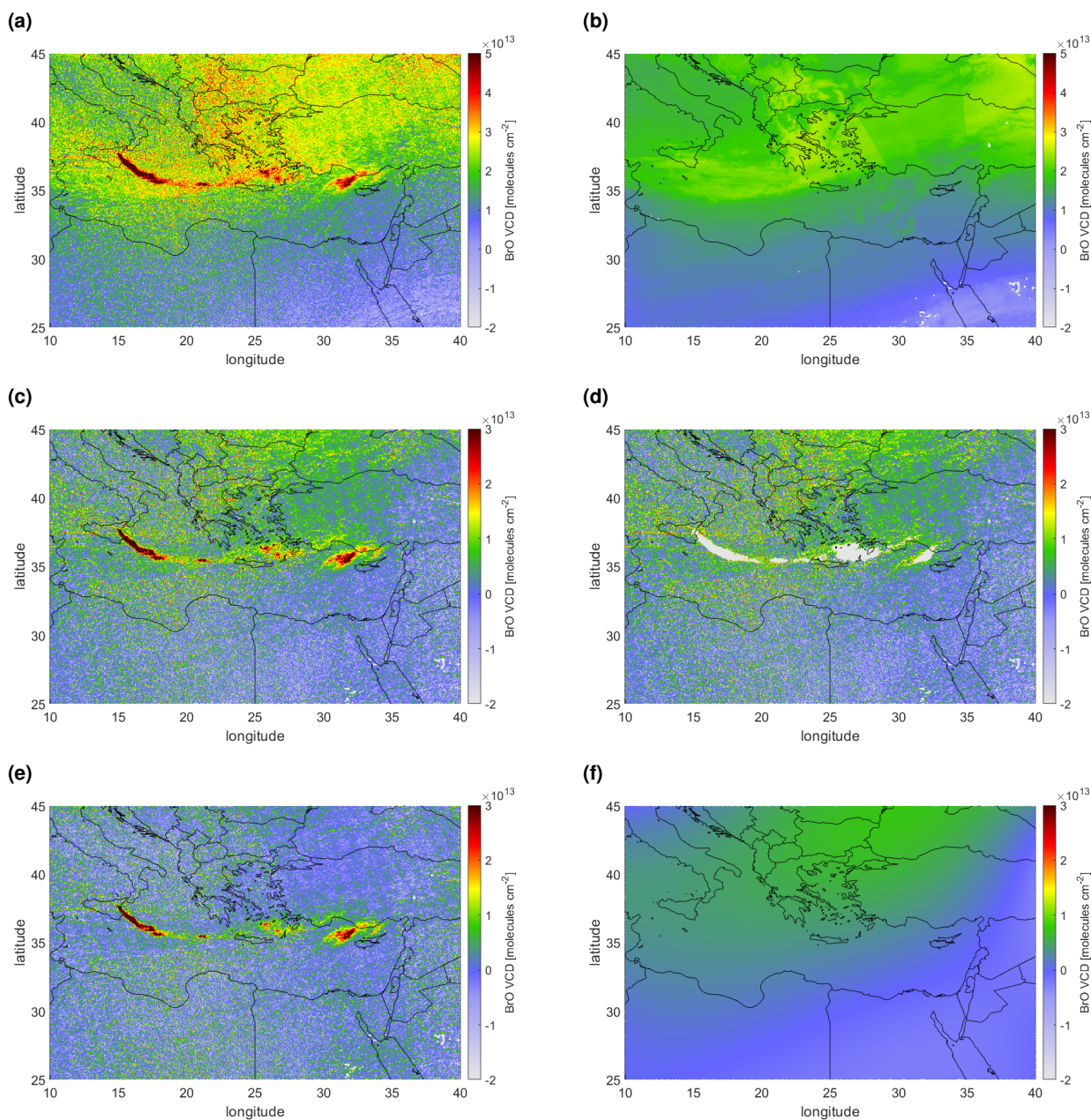
Figure 15. Overview of the processing of the BrO VCD for a volcanic event (Mt. Etna, 25 December 2018): **(a)** The uncorrected data is first corrected using **(b)** the ozone latitude correction term to yield **(c)** the ozone latitude corrected BrO VCD. For the calculation of the spatial polynomial correction **(d)** the masked plume is used and a third order spatial 2D polynomial term is fitted, yielding **(f)** the local background correction BrO map. **(e)** Subtraction from **(c)** yields the final corrected BrO VCD map.

585 is clearly visible in the SO_2 map. This is also the case for BrO, but there are also large gradients visible in the scale of 5×10^{13} molecules cm^{-2}, which is in the order of the volcanic BrO signal itself. The processing steps of the BrO correction scheme is shown in Fig. 15. The uncorrected BrO VCD (shown in panel a) is first corrected using the cloud-ozone correction term (whose correction BrO VCD is shown in panel b), which is derived using the BrO VCDs from the $20°$ latitude band around encompassing the volcano (in this case $25° - 45°$ N). This correction term removes most of the large-scale biases in the

590 BrO map, but also fine structures originating from cloud shielding, resulting in the ozone-latitude corrected BrO VCD map (shown in panel c). Lastly, the volcanic plume is masked based on the SO_2 signal (using a three-σ threshold, panel d) and the the remaining pixel in the region used for a local background correction (the correction term is shown in panel f), resulting in the final BrO VCD (shown in panel e). There, the systematic background features are well reduced.

In the following several examples of different BrO VCD strength and at different latitudes are displayed and discussed in
595 order to show the efficacy of the retrieval in different circumstances.

6.3.1 The plume of Sheveluch, Kamchatka, Russia on 18 April 2019

An example of a small scale eruption at high latitudes is the plume of Sheveluch, Kamtchatka on 18 April 2019. While only low SO_2 VCDs are observed – not exceeding 8×10^{16} molecules cm^{-2} (see Fig. 16a) – there is still a clearly enhanced BrO VCDs visible coinciding with the SO_2 pattern (see Fig. 16b) in the order of several $\times 10^{13}$ molecules cm^{-2}. However, there is
600 also elevated background BrO of up to 3×10^{13} molecules cm^{-2} visible north of the plume over the island. These background structures are clearly identified by the correction term (see Fig. 16d) and the resulting BrO VCD map (see Fig. 16c) shows a smooth background of roughly zero.

It is noteworthy that this is an example where the correction term actually shows a large gradient at the location of the plume (at $57°$ N and $161°$ - $162°$ E) where the correction term varies by more than 5×10^{12} molecules cm^{-2}. This gradient is caused
605 by a cloud edge in this area (see Fig. B1c,d).

6.3.2 The plume of Ambrym volcano, Vanuatu on 30 September 2018

Another minor eruption where a BrO signal is detected is the eruption of Ambrym volcano on 30 September 2018 (see Fig. 17). While the SO_2 signal can be detected over several $100 \, \mathrm{km}$, maximum SO_2 columns do not exceed 1.5×10^{17} molecules cm^{-2} (see Fig. 17a). Nevertheless, BrO VCDs exceed 3×10^{13} molecules cm^{-2} indicating that the volcanic emissions are relatively
610 BrO-rich (see Fig. 17b). In contrast to the high-latitude Sheveluch eruption (see 6.3.1), the BrO background in this case is much weaker (see Fig. 17b), since the plume is located close to the equator where the reference spectrum is taken. Furthermore, there are only low clouds in the area (see Fig. B2d), hence cloud influence is low. Nevertheless, the correction term applies minor corrections for cloudy regions, e. g. for the high cloud at $14°$ S $168°$ E Fig. B2d, where the correction factor accounts for the negative BrO VCD (see Fig. 17d), and slightly homogenizes the background (see Fig. 17c).
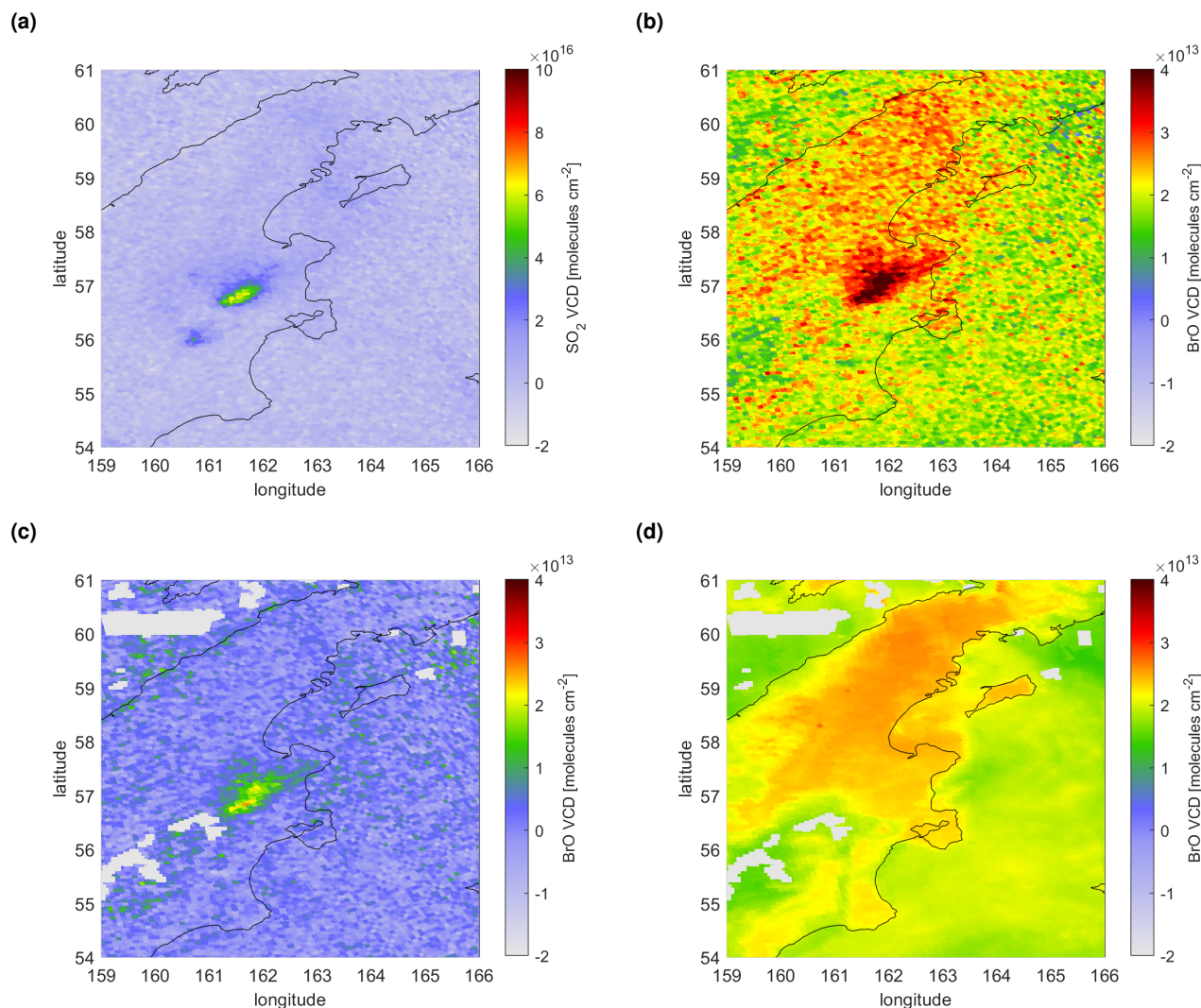
Figure 16. Eruption of Sheveluch, Kamchatka, Russia, on 18 April 2019. **(a)** the SO_2 VCD map, **(b)** the original BrO VCD map, **(c)** the corrected BrO VCD map, and **(d)** the BrO correction term consisting of the lat ozone BrO correction and the local background correction.

6.3.3 The eruption of Mt. Etna, Italy on 29 January 2019

An example for a medium eruption, with a very localized volcanic plume is the Mt. Etna eruption on 29 January 2019 (see Fig. 18). This eruption is part of a phase of eruptive activity which started with weak degassing in December 2018 culminating in an explosive VEI-2 eruption on 24 December 2018 (Calvari et al., 2020) accompanied by lava flows (GVP, 2019). Activity subsided to strombolian activity throughout January and February 2019 (GVP, 2019). The eruptive event on 29 January 2019 falls within a week of increased activity during the last week of January (GVP, 2019). The event is a medium eruption, with maximum SO_2 VCD of $5 \times 10^{17}\,\mathrm{molecules\,cm^{-2}}$, but with a very localized plume (see Fig. 18a). SO_2 VCDs exceeding

34

(a)

(b)

(c)

(d)
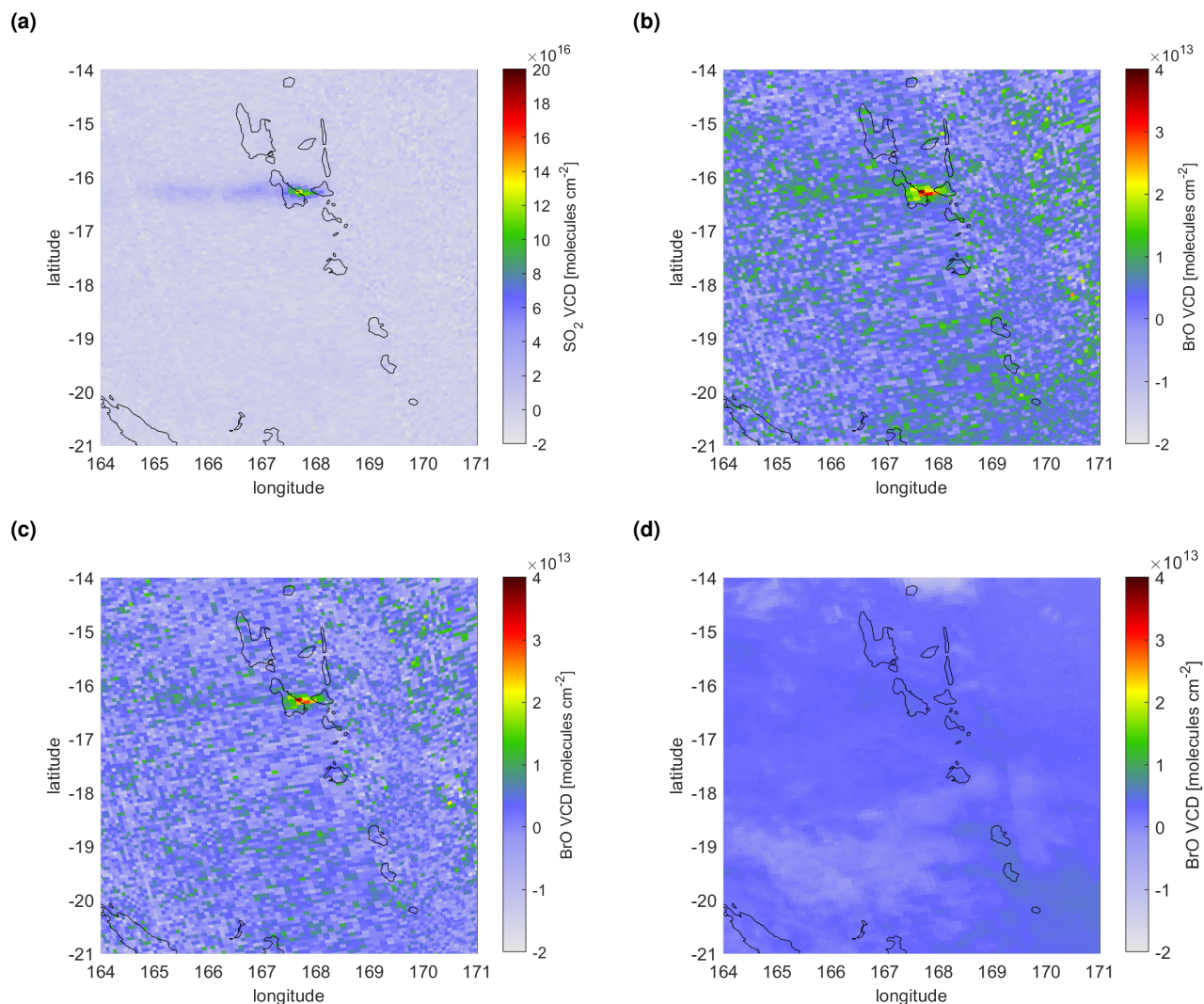
Figure 17. Eruption of Ambrym volcano, Vanuatu, on 30 September 2018. **(a)** the SO_2 VCD map, **(b)** the original BrO VCD map, **(c)** the corrected BrO VCD map, and **(d)** the BrO correction term consisting of the lat ozone BrO correction and the local background correction.

$1 \times 10^{17}\,\mathrm{molecules\,cm^{-2}}$ only occur within the first $50\,\mathrm{km}$ downwind from the volcano. A clear BrO signal of up to $8 \times 10^{13}\,\mathrm{molecules\,cm^{-2}}$ is also only observed in this area around the volcano (see Fig. 18b, exceeding the upper boundary of the colormap scale). Further downwind only a very faint positive BrO signal can be seen. The background signal is in the order of $2 \times 10^{13}\,\mathrm{molecules\,cm^{-2}}$ is well matched by the correction term (see Fig. 18d), yielding the corrected BrO VCD map (see Fig. 18c), where both the strong signal at the volcano and the weaker outflow is visible.

625

(a)

(b)

(c)

(d)
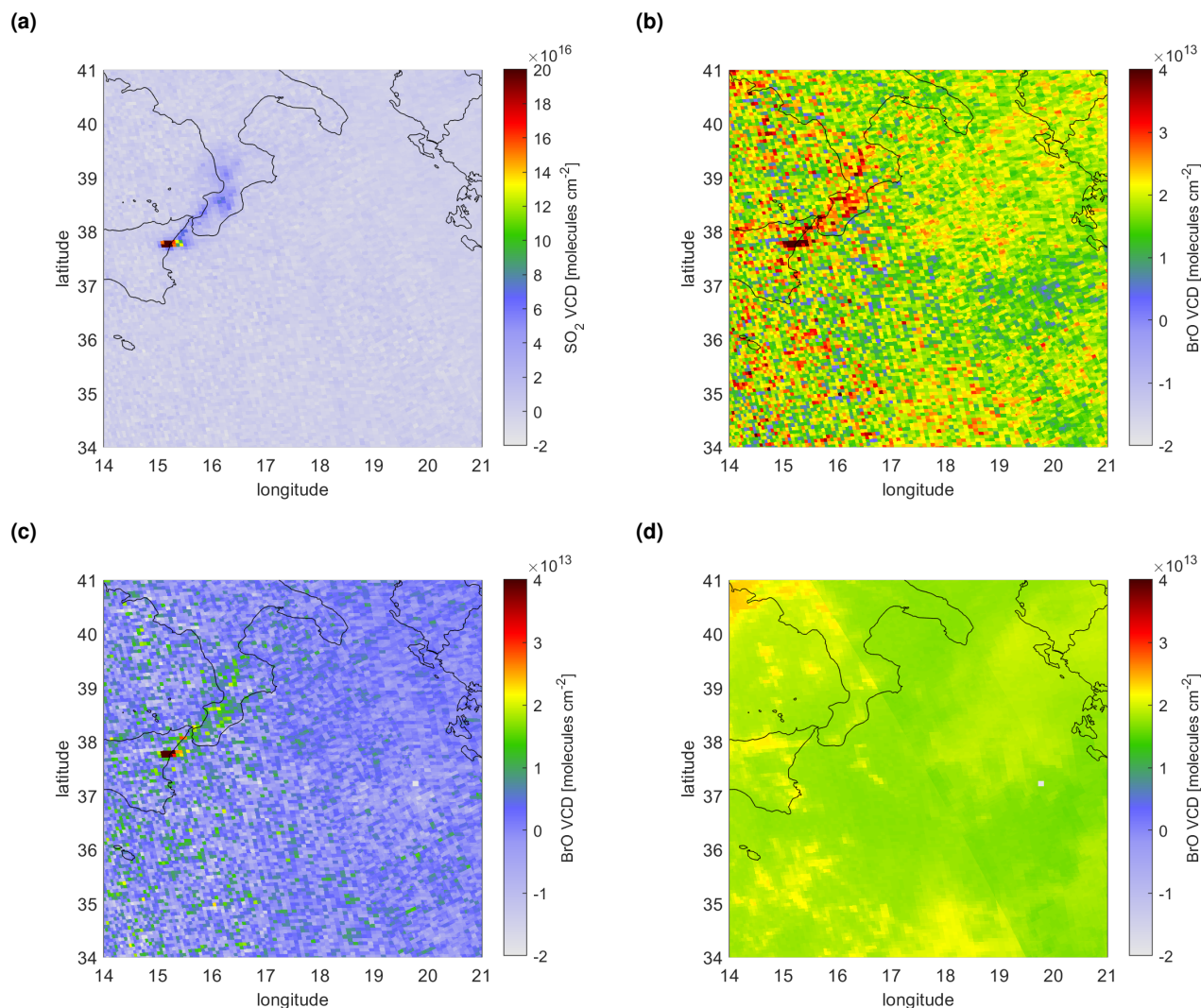
Figure 18. Eruption of Mount Etna, Italy, on 29 January 2019. **(a)** the SO_2 VCD map, **(b)** the original BrO VCD map, **(c)** the corrected BrO VCD map, and **(d)** the BrO correction term consisting of the lat ozone BrO correction and the local background correction.

7 Conclusions

We present a new retrieval scheme designed specifically for the accurate detection of BrO inside minor volcanic plumes from satellite spectra. Expanding the DOAS fit wavelength range to lower wavelength of $323\,nm$ and thus a fit range of $323 - 360\,nm$ reduces the statistical uncertainty, without increasing any systematic influences. This is made possible by the introduction of so called »Pukite« terms (Pukīte et al., 2010), which account for second order effects of the strong absorption of O_3 at lower wavelengths. In addition, this wavelength range was shown to be least susceptible for a systematic influence caused by inter-

ference due to HCHO. While no systematic bias is found for HCHO columns $< 2 \times 10^{16}\,\mathrm{molecules\,cm^{-2}}$, HCHO columns between 2 and $4 \times 10^{16}\,\mathrm{molecules\,cm^{-2}}$ could introduce a positive BrO VCD bias of roughly $2.5 \times 10^{12}\,\mathrm{molecules\,cm^{-2}}$.

635 Secondly, we propose a sophisticated, empirical correction scheme for the non-volcanic BrO background, based on cloud fraction, cloud altitude, as well as on the O_3 VCD, all correlating with spatially distinct patterns in the BrO VCD map. The origin of the cloud effect is not clear. Possible effects can be partially shielding of the tropospheric BrO column, but also non-linear spectroscopic effects. O_3 is indicative for a change in the BrO stratospheric column. A combined empirical multi-dimensional polynomial including cloud fraction, cloud height and the measured O_3 VCD applied to the latitude band of the

640 volcanic plume location proves to best account for these structures. This correction scheme reduces the systematic influence at the equator by one order of magnitude from $1 \times 10^{13}\,\mathrm{molecules\,cm^{-2}}$ to $1 \times 10^{12}\,\mathrm{molecules\,cm^{-2}}$.

The statistical uncertainty of the retrieved BrO VCD is found to be roughly $6.5 \times 10^{12}\,\mathrm{molecules\,cm^{-2}}$, thus at least a factor of two larger than the systematic effects. Compared to other recent BrO DOAS fitting schemes (Sihler et al., 2012; Hörmann et al., 2013) the statistical noise is reduced by a factor of up to 1.8, mainly due to the use of the larger wavelength fit range of

645 $323 - 360\,\mathrm{nm}$. It is noteworthy, that averaging over longer periods of time could further reduce the statistical variation.

In several example volcanic plumes we show, that the developed background correction scheme successfully removes BrO background gradients. In combination with the precise BrO DOAS retrieval, this leads to the more accurate detection of BrO than for previous retrievals even in volcanic plumes during minor eruptive activity.

The algorithm developed here will allow much more detailed investigation of volcanic BrO and the volcanic BrO/SO$_2$ ratio

650 on a global scale.

Appendix A: Detailed data for systematic influences

A1   Cloud and ozone influences

BrO VCD as a function of CF and CH at the equatorial region on 1 October 2018 for all eight fit settings (see Fig. A1). The relation is stronger for larger fit wavelength ranges (left side) and seems also slightly increased for fits including HCHO (bottom row). The response is weakest for the fits with wavelength range $332 - 360\,\text{nm}$ both for *SR* and *HCHO* fits.
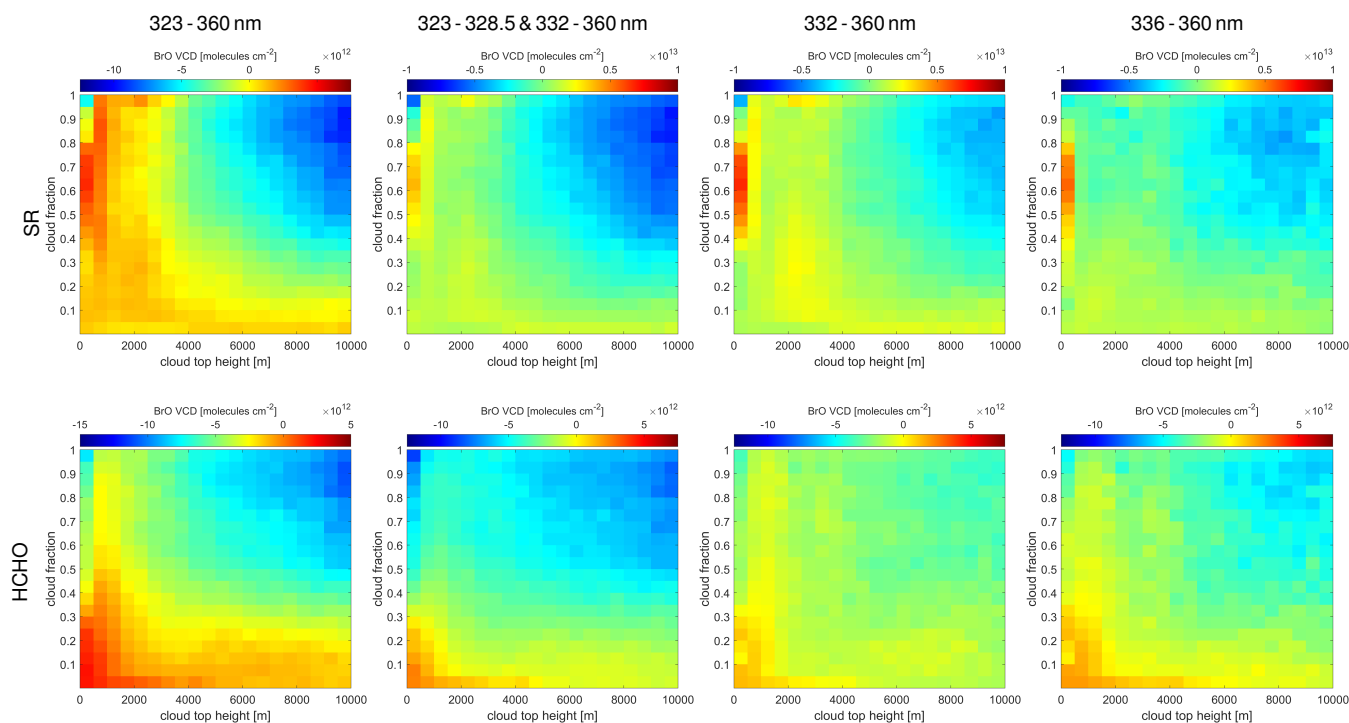

Figure A1. Mean BrO VCD dependency on the cloud height – cloud fraction bins for the equatorial region [$\pm 20°$ N, $\pm 180°$ E] for the eight different BrO fits. Top row: Fits not including HCHO absorption cross section (*SR*), fit ranges: *323-360 nm*, *323-328.5 & 332-360 nm*, *332-360 nm*, *336-360 nm* (f. l. t. r). Bottom row: Fits including the HCHO absorption cross section (*HCHO*), for each fit range from the top row respectively.

655

38

A2 Cloud and ozone correction scheme

Fig. A2 shows the correction terms for the three different ozone cloud correction schemes. The corresponding corrected BrO VCD maps are shown in Fig. 7.

(a)

(b)

(c)
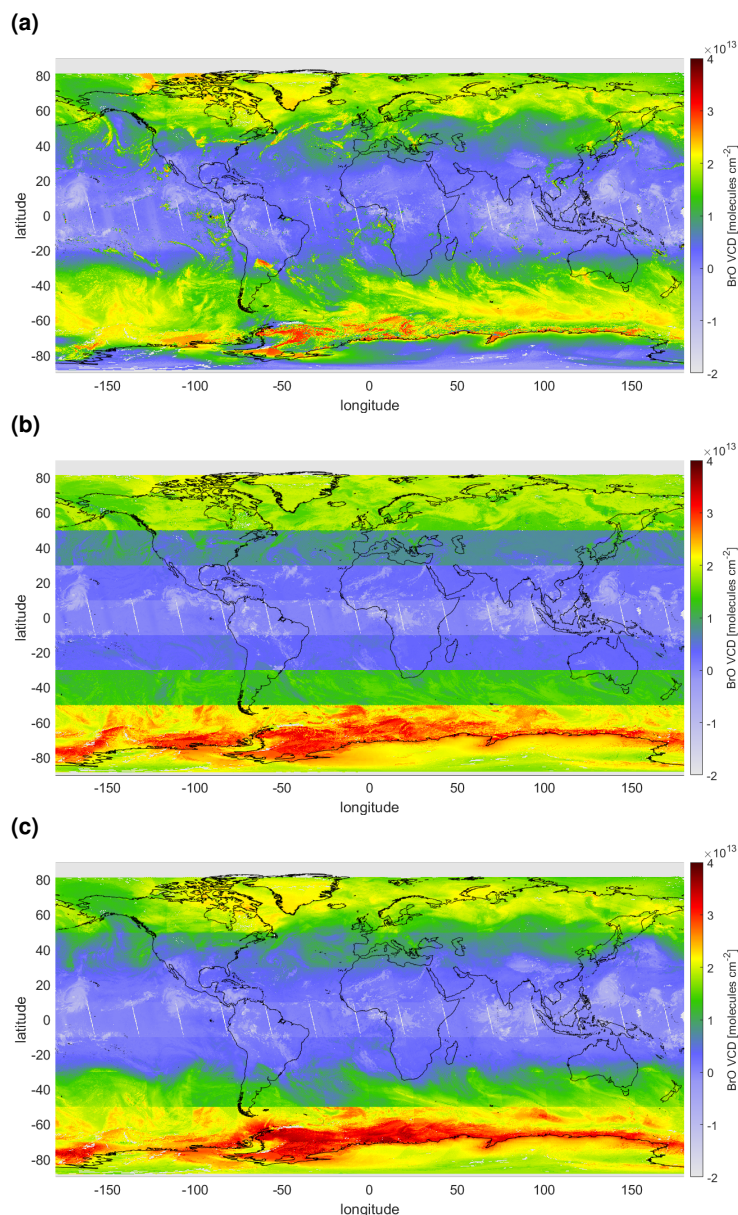
Figure A2. Global map of the correction term of the three correction schemes for the *SR 323 - 360 nm* fit: **(a)** »ozone« **(b)** »latitude«, and **(c)** »ozone latitude« correction schemes. The BrO VCD map prior to correction is plotted in Fig. 3, and the corresponding corrected maps for all three schemes is plotted in Fig. 7.

A3 Influence of formaldehyde

Fig. A3 shows the mean BrO SCD seperated by the HCHO-CF bins for each of the eight fit settings of the African biomass burning region.
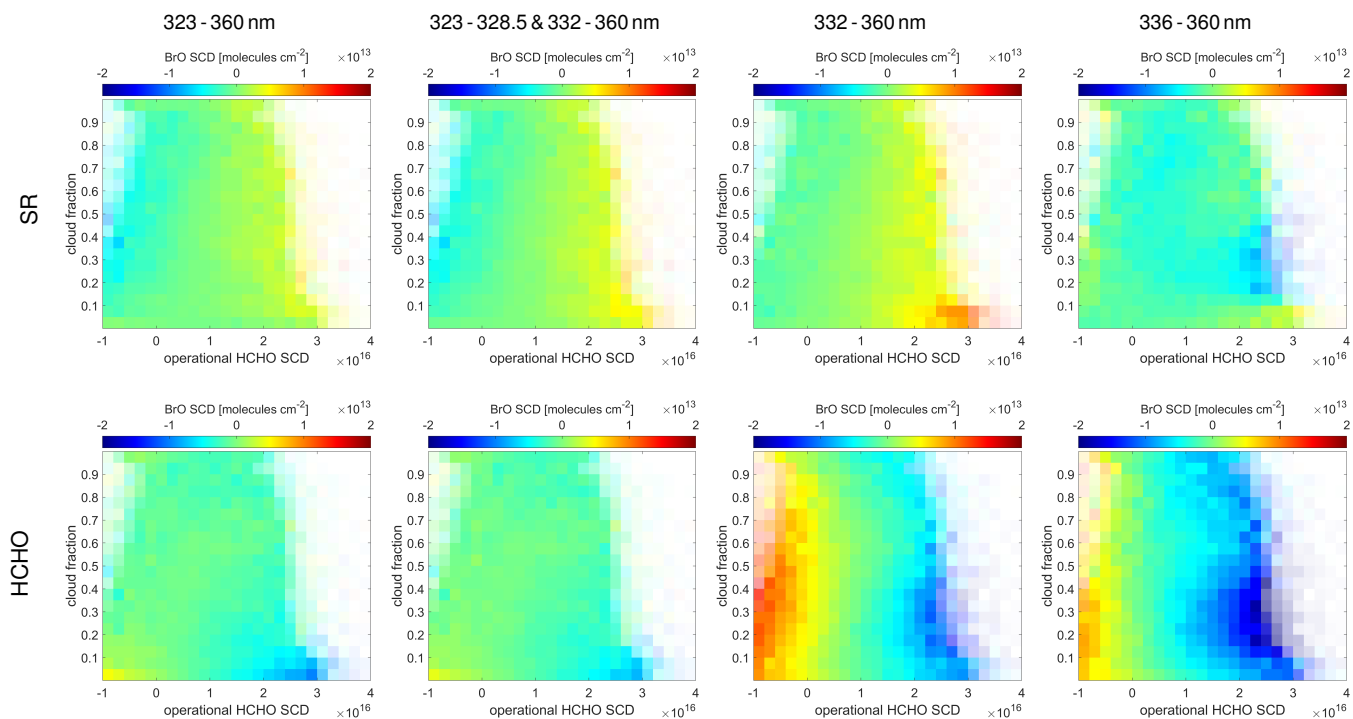
Figure A3. Mean BrO SCD as a function cloud fraction and HCHO SCD bins for the African biomass region on 1 October 2018 for the four different fit ranges (from left to right): *323 - 360 nm, 323 - 328.5 & 332 - 360 nm, 332 - 360 nm*, and *336 - 360 nm*. *Upper row*: fits excluding HCHO (*SR*); *lower row*: fits including HCHO (*HCHO*).

660

Appendix B: Additional data for the example eruptions

In this section the auxiliary data used for the cloud-ozone correction scheme are shown for every example eruption detailed in Sect. 6.3. All plots include the SO_2 map to indicate the plume dispersion pattern and the O_3 VCD as well as the FRESCO cloud height and cloud fraction, all three used as input for the cloud-ozone correction scheme.
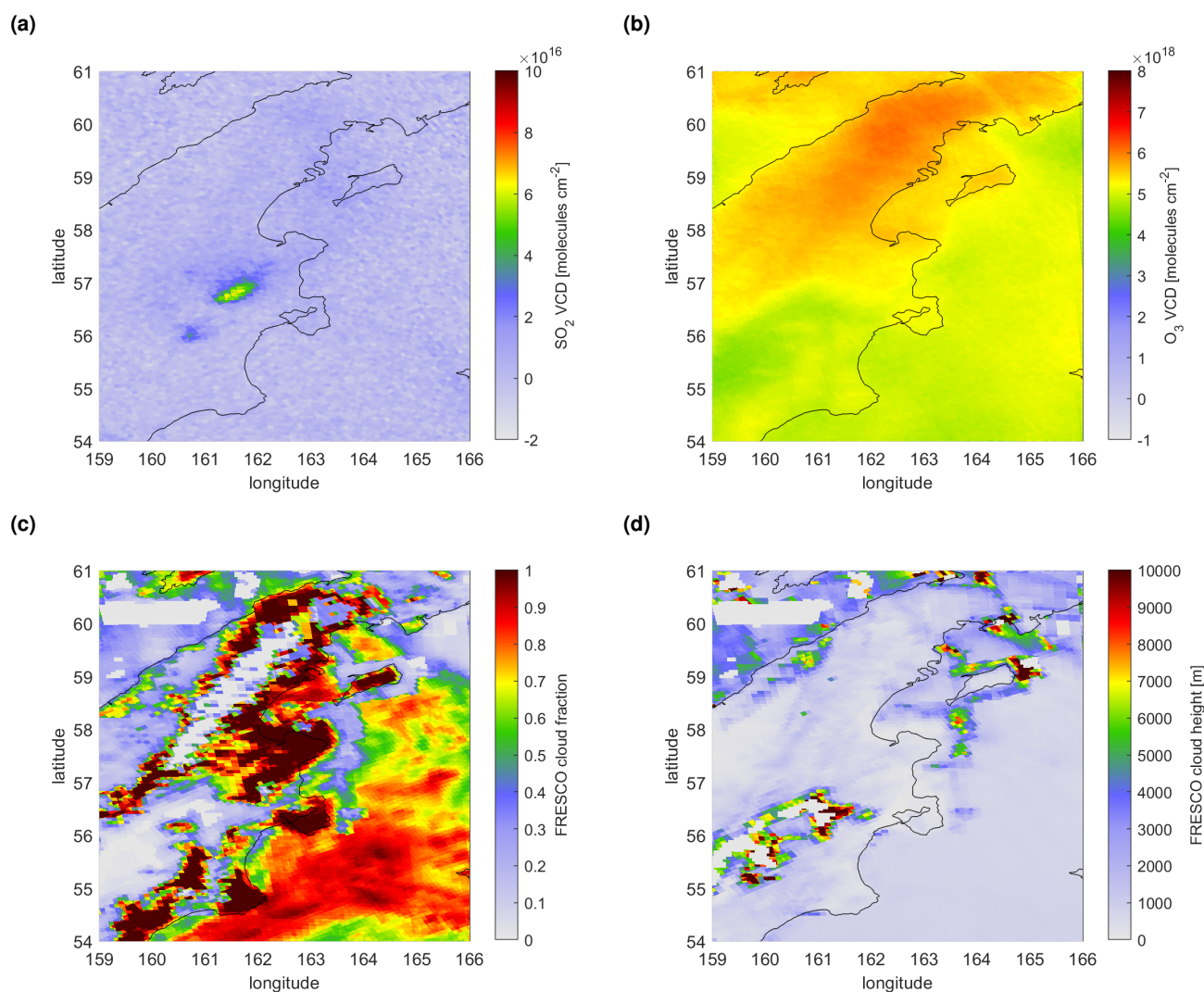
Figure B1. Auxiliary data used for correction scheme for the eruption of Sheveluch, Kamchatka, Russia, on 18 April 2019. Maps of **(a)** the SO_2 VCD, **(b)** the O_3 VCD, **(c)** the FRESCO cloud fraction, and **(d)** the FRESCO cloud height. The corresponding uncorrected and corrected BrO VCD map and the BrO background correction map can be found in Fig. 16.
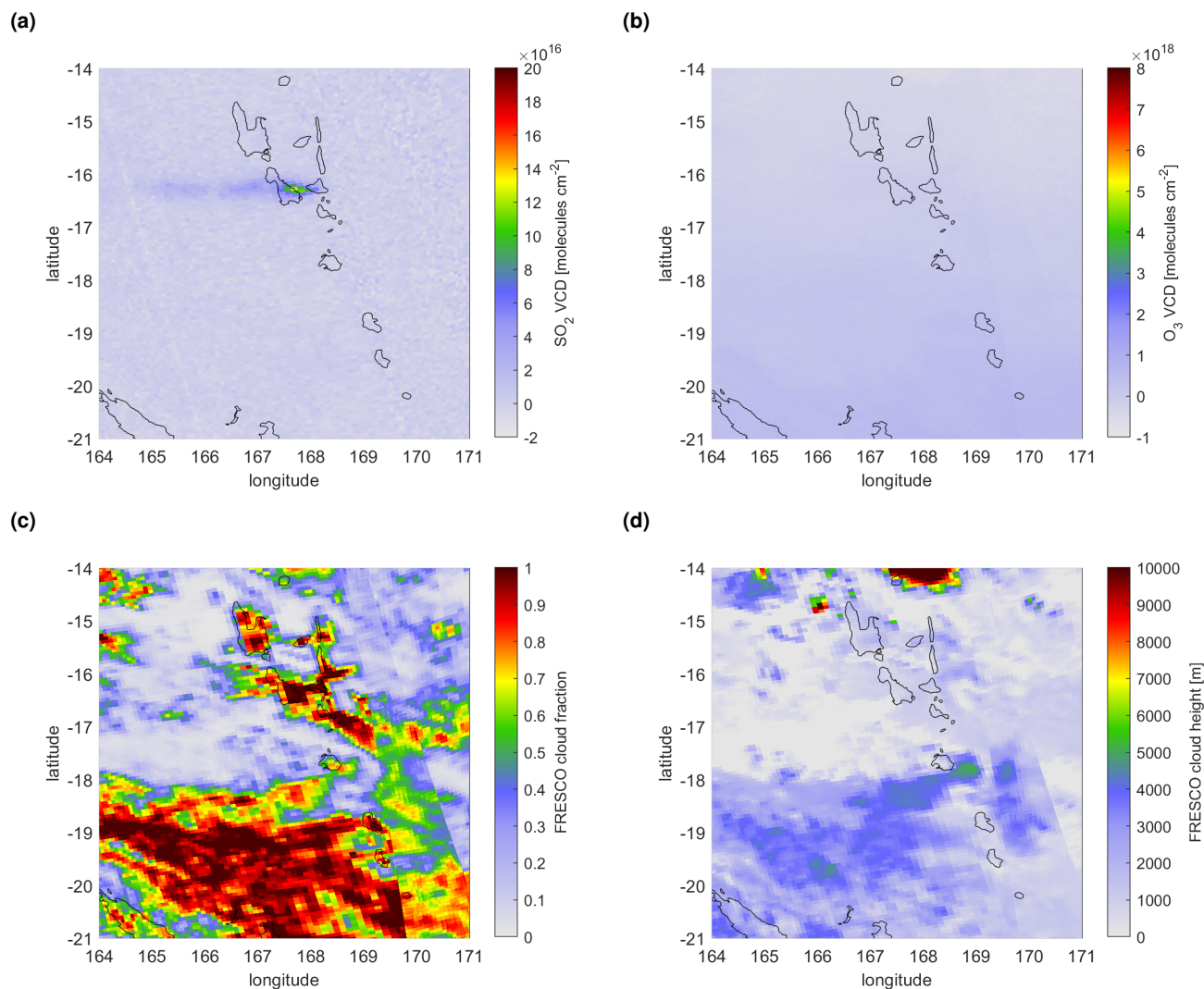
Figure B2. Auxiliary data used for correction scheme for the eruption of Ambrym, Vanuatu, on 30 September 2018. Maps of **(a)** the SO_2 VCD, **(b)** the O_3 VCD, **(c)** the FRESCO cloud fraction, and **(d)** the FRESCO cloud height. The corresponding uncorrected and corrected BrO VCD map and the BrO background correction map can be found in Fig. 17.
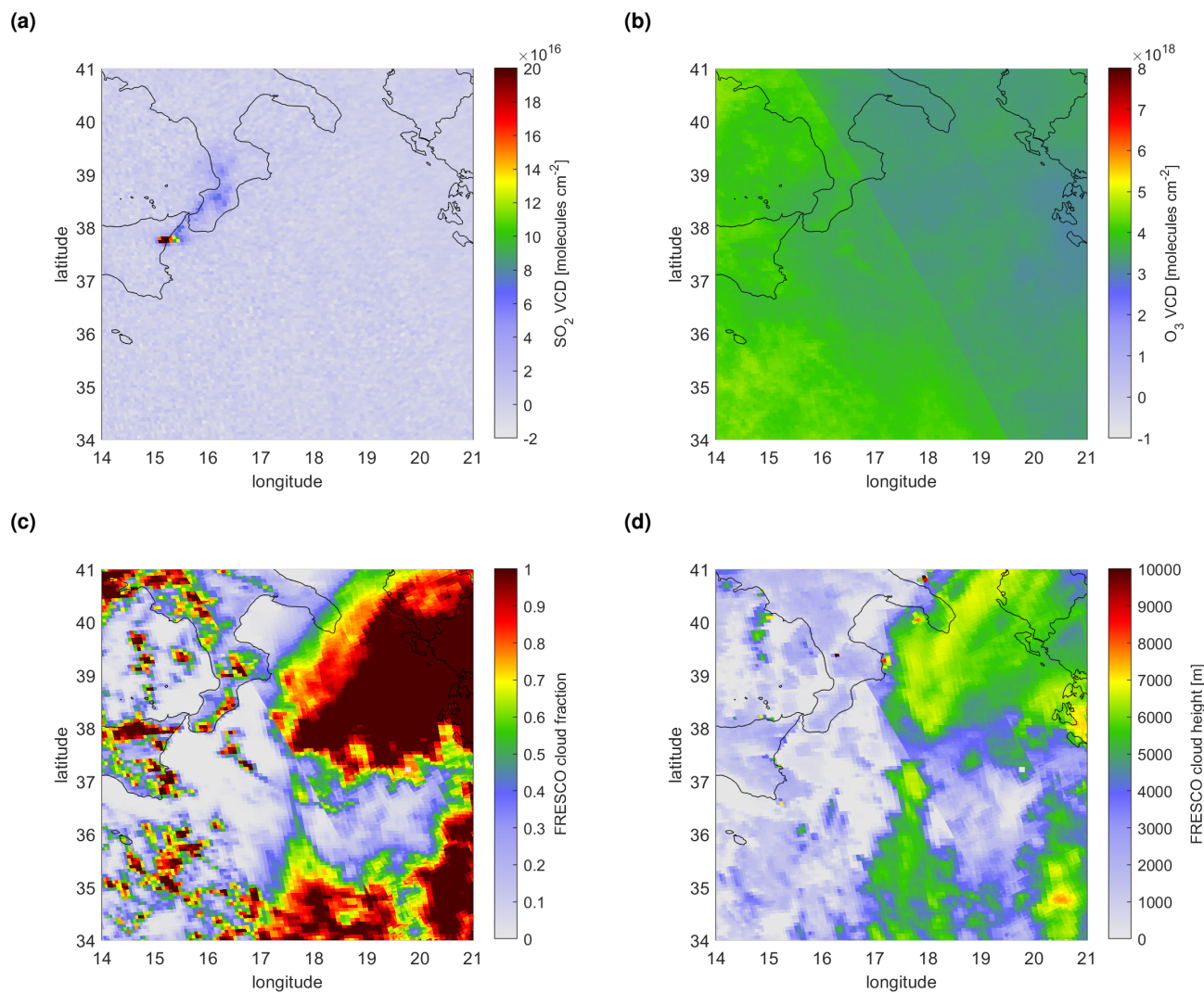
Figure B3. Auxiliary data used for correction scheme for the eruption of Mount Etna, Italy, on 29 January 2019. Maps of **(a)** the SO_2 VCD, **(b)** the O_3 VCD, **(c)** the FRESCO cloud fraction, and **(d)** the FRESCO cloud height. The corresponding uncorrected and corrected BrO VCD map and the BrO background correction map can be found in Fig. 18.

References

Global Volcanism Program, 2010. Report on Etna (Italy), Bulletin of the Global Volcanism Network, 44, https://doi.org/10.5479/si.gvp.bgvn201904-211060, 2019.

Copernicus Sentinel-5P (processed by ESA), 2021, TROPOMI Level 2 Nitrogen Dioxide total column products. Version 02. European Space Agency, 2021.

Afe, O. T., Richter, A., Sierk, B., Wittrock, F., and Burrows, J. P.: BrO emission from volcanoes: A survey using GOME and SCIAMACHY measurements, Geophysical Research Letters, 31, https://doi.org/10.1029/2004GL020994, 2004.

Barrie, L. A., Bottenheim, J. W., Schnell, R. C., Crutzen, P. J., and Rasmussen, R. A.: Ozone destruction and photochemical reactions at polar sunrise in the lower Arctic atmosphere, Nature, 334, 138–141, https://doi.org/10.1038/334138a0, 1988.

Begoin, M., Richter, A., Weber, M., Kaleschke, L., Tian-Kunze, X., Stohl, A., Theys, N., and Burrows, J. P.: Satellite observations of long range transport of a large BrO plume in the Arctic, Atmospheric Chemistry and Physics, 10, 6515–6526, https://doi.org/10.5194/acp-10-6515-2010, 2010.

Beirle, S., Sihler, H., and Wagner, T.: Linearisation of the effects of spectral shift and stretch in DOAS analysis, Atmospheric Measurement Techniques, 6, 661–675, https://doi.org/10.5194/amt-6-661-2013, 2013.

Beirle, S., Lampel, J., Lerot, C., Sihler, H., and Wagner, T.: Parameterizing the instrumental spectral response function and its changes by a super-Gaussian and its derivatives, Atmospheric Measurement Techniques, 10, 581–598, https://doi.org/10.5194/amt-10-581-2017, 2017.

Bobrowski, N. and Giuffrida, G.: Bromine monoxide / sulphur dioxide ratios in relation to volcanological observations at Mt. Etna 2006 - 2009, Solid Earth, 3, 433–445, https://doi.org/10.5194/se-3-433-2012, 2012.

Bobrowski, N. and Platt, U.: SO_2/BrO ratios studied in five volcanic plumes, Journal of Volcanology and Geothermal Research, 166, 147 – 160, https://doi.org/10.1016/j.jvolgeores.2007.07.003, 2007.

Bobrowski, N., Hönniger, G., Galle, B., and Platt, U.: Detection of bromine monoxide in a volcanic plume, Nature, 423, 273–276, https://doi.org/10.1038/nature01625, 2003.

Bobrowski, N., von Glasow, R., Giuffrida, G. B., Tedesco, D., Aiuppa, A., Yalire, M., Arellano, S., Johansson, M., and Galle, B.: Gas emission strength and evolution of the molar ratio of BrO/SO_2 in the plume of Nyiragongo in comparison to Etna, Journal of Geophysical Research: Atmospheres, 120, 277–291, https://doi.org/10.1002/2013jd021069, 2015.

Boersma, K. F., Eskes, H. J., Dirksen, R. J., van der A, R. J., Veefkind, J. P., Stammes, P., Huijnen, V., Kleipool, Q. L., Sneep, M., Claas, J., Leitão, J., Richter, A., Zhou, Y., and Brunner, D.: An improved tropospheric NO_2 column retrieval algorithm for the Ozone Monitoring Instrument, Atmospheric Measurement Techniques, 4, 1905–1928, https://doi.org/10.5194/amt-4-1905-2011, 2011.

Bogumil, K., Orphal, J., Homann, T., Voigt, S., Spietz, P., Fleischmann, O. C., Vogel, A., Hartmann, M., Kromminga, H., Bovensmann, H., Frerick, J., and Burrows, J. P.: Measurements of molecular absorption spectra with the SCIAMACHY pre-flight model: instrument characterization and reference data for atmospheric remote-sensing in the 230–2380 nm region, Journal of Photochemistry and Photobiology A: Chemistry, 157, 167–184, https://doi.org/10.1016/S1010-6030(03)00062-5, atmospheric Photochemistry, 2003.

Borger, C., Beirle, S., Dörner, S., Sihler, H., and Wagner, T.: Total column water vapour retrieval from S-5P/TROPOMI in the visible blue spectral range, Atmospheric Measurement Techniques, 13, 2751–2783, https://doi.org/10.5194/amt-13-2751-2020, 2020.

Bougoudis, I., Blechschmidt, A.-M., Richter, A., Seo, S., Burrows, J. P., Theys, N., and Rinke, A.: Long-term time series of Arctic tropospheric BrO derived from UV–VIS satellite remote sensing and its relation to first-year sea ice, Atmospheric Chemistry and Physics, 20, 11 869–11 892, https://doi.org/10.5194/acp-20-11869-2020, 2020.

715   Brenna, H., Kutterolf, S., and Krüger, K.: Global ozone depletion and increase of UV radiation caused by pre-industrial tropical volcanic eruptions, Scientific Reports, 9, https://doi.org/10.1038/s41598-019-45630-0, 2019.

Burrows, J. P., Borrell, P., and Platt, U., eds.: The Remote Sensing of Tropospheric Composition from Space, Springer Berlin Heidelberg, https://doi.org/10.1007/978-3-642-14791-3, 2011.

Calvari, S., Bilotta, G., Bonaccorso, A., Caltabiano, T., Cappello, A., Corradino, C., Negro, C. D., Ganci, G., Neri, M., Pecora, E., Salerno,

720   G. G., and Spampinato, L.: The VEI 2 Christmas 2018 Etna Eruption: A Small But Intense Eruptive Event or the Starting Phase of a Larger One?, Remote Sensing, 12, 905, https://doi.org/10.3390/rs12060905, 2020.

Carn, S. A., Fioletov, V. E., McLinden, C. A., Li, C., and Krotkov, N. A.: A decade of global volcanic SO2 emissions measured from space, Scientific Reports, 7, https://doi.org/10.1038/srep44095, 2017.

Chance, K.: Analysis of BrO measurements from the Global Ozone Monitoring Experiment, Geophysical Research Letters, 25, 3335–3338,

725   https://doi.org/10.1029/98GL52359, 1998.

Chance, K.: Algorithm Theoretical Basis Document - Volume IV, Tech. rep., Smithsonian Astrophysical Observatory, Cambridge, MA, USA, 2002.

Chance, K.: OMBRO—OMHCHO—OMOCLO De-Striping README FILE, Tech. rep., https://ozoneaq.gsfc.nasa.gov/media/docs/OMSAO_DeStriping_README.pdf, 2007.

730   Compernolle, S., Argyrouli, A., Lutz, R., Sneep, M., Lambert, J.-C., Fjæraa, A. M., Hubert, D., Keppens, A., Loyola, D., O'Connor, E., Romahn, F., Stammes, P., Verhoelst, T., and Wang, P.: Validation of the Sentinel-5 Precursor TROPOMI cloud data with Cloudnet, Aura OMI O_2–O_2, MODIS, and Suomi-NPP VIIRS, Atmospheric Measurement Techniques, 14, 2451–2476, https://doi.org/10.5194/amt-14-2451-2021, 2021.

De Smedt, I., Theys, N., Yu, H., Danckaert, T., Lerot, C., Compernolle, S., Van Roozendael, M., Richter, A., Hilboll, A., Peters, E., Ped-

735   ergnana, M., Loyola, D., Beirle, S., Wagner, T., Eskes, H., van Geffen, J., Boersma, K. F., and Veefkind, P.: Algorithm theoretical baseline for formaldehyde retrievals from S5P TROPOMI and from the QA4ECV project, Atmospheric Measurement Techniques, 11, 2395–2426, https://doi.org/10.5194/amt-11-2395-2018, 2018.

Dinger, F., Bobrowski, N., Warnach, S., Bredemeyer, S., Hidalgo, S., Arellano, S., Galle, B., Platt, U., and Wagner, T.: Periodicity in the BrO/SO_2 molar ratios in the volcanic gas plume of Cotopaxi and its correlation with the Earth tides during the eruption in 2015, Solid

740   Earth, 9, 247–266, https://doi.org/10.5194/se-9-247-2018, 2018.

Eisinger, M. and Burrows, J. P.: Tropospheric sulfur dioxide observed by the ERS-2 GOME instrument, Geophysical Research Letters, 25, 4177–4180, https://doi.org/https://doi.org/10.1029/1998GL900128, 1998.

Fioletov, V. E., McLinden, C. A., Krotkov, N., Li, C., Joiner, J., Theys, N., Carn, S., and Moran, M. D.: A global catalogue of large SO_2 sources and emissions derived from the Ozone Monitoring Instrument, Atmospheric Chemistry and Physics, 16, 11 497–11 519,

745   https://doi.org/10.5194/acp-16-11497-2016, 2016.

Fleischmann, O. C., Hartmann, M., Burrows, J. P., and Orphal, J.: New ultraviolet absorption cross-sections of BrO at atmospheric temperatures measured by time-windowing Fourier transform spectroscopy, Journal of Photochemistry and Photobiology A: Chemistry, 168, 117–132, https://doi.org/10.1016/j.jphotochem.2004.03.026, 2004.

Hegels, E., Crutzen, P. J., Klüpfel, T., Perner, D., and Burrows, J. P.: Global distribution of atmospheric bromine-monoxide from GOME on

750   Earth Observing Satellite ERS-2, Geophysical Research Letters, 25, 3127–3130, https://doi.org/10.1029/98GL02417, 1998.

Herrmann, M., Schöne, M., Borger, C., Warnach, S., Wagner, T., Platt, U., and Gutheil, E.: Ozone depletion events in the Arctic spring of 2019: a new modeling approach to bromine emissions, Atmospheric Chemistry and Physics, 22, 13 495–13 526, https://doi.org/10.5194/acp-22-13495-2022, 2022.

Heue, K.-P., Brenninkmeijer, C. A. M., Baker, A. K., Rauthe-Schöch, A., Walter, D., Wagner, T., Hörmann, C., Sihler, H., Dix, B., Frieß, U., Platt, U., Martinsson, B. G., van Velthoven, P. F. J., Zahn, A., and Ebinghaus, R.: SO_2 and BrO observation in the plume of the Eyjafjallajökull volcano 2010: CARIBIC and GOME-2 retrievals, Atmospheric Chemistry and Physics, 11, 2973–2989, https://doi.org/10.5194/acp-11-2973-2011, 2011.

Hörmann, C., Sihler, H., Bobrowski, N., Beirle, S., Penning de Vries, M., Platt, U., and Wagner, T.: Systematic investigation of bromine monoxide in volcanic plumes from space by using the GOME-2 instrument, Atmospheric Chemistry and Physics, 13, 4749–4781, https://doi.org/10.5194/acp-13-4749-2013, 2013.

Hörmann, C., Sihler, H., Beirle, S., Penning de Vries, M., Platt, U., and Wagner, T.: Seasonal variation of tropospheric bromine monoxide over the Rann of Kutch salt marsh seen from space, Atmospheric Chemistry and Physics, 16, 13 015–13 034, https://doi.org/10.5194/acp-16-13015-2016, 2016.

Hörmann, C.: Space-based monitoring of volcanic emissions using the GOME-2 instrument, Ph.D. thesis, Heidelberg University, https://doi.org/10.11588/HEIDOK.00014536, 2013.

Kern, C., Sihler, H., Vogel, L., Rivera, C., Herrera, M., and Platt, U.: Halogen oxide measurements at Masaya Volcano, Nicaragua using active long path differential optical absorption spectroscopy, Bulletin of Volcanology, 71, 659–670, https://doi.org/10.1007/s00445-008-0252-8, 2009.

Khokhar, M. F., Frankenberg, C., Van Roozendael, M., Beirle, S., Kühl, S., Richter, A., Platt, U., and Wagner, T.: Satellite observations of atmospheric SO2 from volcanic eruptions during the time-period of 1996–2002, Advances in Space Research, 36, 879–887, https://doi.org/10.1016/j.asr.2005.04.114, atmospheric Remote Sensing: Earth's Surface, Troposphere, Stratosphere and Mesosphere- I, 2005.

Latsch, M., Richter, A., Eskes, H., Sneep, M., Wang, P., Veefkind, P., Lutz, R., Loyola, D., Argyrouli, A., Valks, P., Wagner, T., Sihler, H., van Roozendael, M., Theys, N., Yu, H., Siddans, R., and Burrows, J. P.: Intercomparison of Sentinel-5P TROPOMI cloud products for tropospheric trace gas retrievals, Atmospheric Measurement Techniques, 15, 6257–6283, https://doi.org/10.5194/amt-15-6257-2022, 2022.

Lübcke, P., Bobrowski, N., Arellano, S., Galle, B., Garzón, G., Vogel, L., and Platt, U.: BrO/SO_2 molar ratios from scanning DOAS measurements in the NOVAC network, Solid Earth, 5, 409–424, https://doi.org/10.5194/se-5-409-2014, 2014.

Meller, R. and Moortgat, G. K.: Temperature dependence of the absorption cross sections of formaldehyde between 223 and 323 K in the wavelength range 225 - 375 nm, Journal of Geophysical Research: Atmospheres, 105, 7089–7101, https://doi.org/10.1029/1999JD901074, 2000.

Perner, D. and Platt, U.: Detection of nitrous acid in the atmosphere by differential optical absorption, Geophysical Research Letters, 6, 917–920, https://doi.org/10.1029/GL006i012p00917, 1979.

Pukīte, J. and Wagner, T.: Quantification and parametrization of non-linearity effects by higher-order sensitivity terms in scattered light differential optical absorption spectroscopy, Atmospheric Measurement Techniques, 9, 2147–2177, https://doi.org/10.5194/amt-9-2147-2016, 2016.

Pukīte, J., Kühl, S., Deutschmann, T., Platt, U., and Wagner, T.: Extending differential optical absorption spectroscopy for limb measurements in the UV, Atmospheric Measurement Techniques, 3, 631–653, https://doi.org/10.5194/amt-3-631-2010, 2010.

Richter, A. and Wagner, T.: Diffuser plate spectral structures and their influence on GOME slant columns, Technical Note to ESA, www.iup.
790 uni-bremen.de/gome/data/diffuser_gome.pdf, 2001.

Richter, A., Wittrock, F., Eisinger, M., and Burrows, J. P.: GOME observations of tropospheric BrO in northern hemispheric spring and
summer 1997, Geophysical Research Letters, 25, 2683–2686, https://doi.org/10.1029/98GL52016, 1998.

Richter, A., Wittrock, F., Ladstätter-Weißenmayer, A., and Burrows, J. P.: Gome measurements of stratospheric and tropospheric BrO,
Advances in Space Research, 29, 1667–1672, https://doi.org/10.1016/S0273-1177(02)00123-0, 2002.

795 Rix, M., Valks, P., Hao, N., Loyola, D., Schlager, H., Huntrieser, H., Flemming, J., Koehler, U., Schumann, U., and Inness, A.: Volcanic SO2,
BrO and plume height estimations using GOME-2 satellite measurements during the eruption of Eyjafjallajökull in May 2010, Journal of
Geophysical Research: Atmospheres, 117, https://doi.org/10.1029/2011JD016718, 2012.

Schöne, M.: Tropospheric BrO plumes in Arctic spring – A comparison of TROPOMI satellite observations and model results, Ph.D. thesis,
Heidelberg University, https://doi.org/10.11588/HEIDOK.00032838, 2023.

800 Seo, S., Richter, A., Blechschmidt, A.-M., Bougoudis, I., and Burrows, J. P.: First high-resolution BrO column retrievals from TROPOMI,
Atmospheric Measurement Techniques, 12, 2913–2932, https://doi.org/10.5194/amt-12-2913-2019, 2019.

Serdyuchenko, A., Gorshelev, V., Weber, M., Chehade, W., and Burrows, J. P.: High spectral resolution ozone absorption cross-sections –
part 2: Temperature dependence, Atmospheric Measurement Techniques, 7, 625–636, https://doi.org/10.5194/amt-7-625-2014, 2014.

Sihler, H., Platt, U., Beirle, S., Marbach, T., Kühl, S., Dörner, S., Verschaeve, J., Frieß, U., Pöhler, D., Vogel, L., Sander, R., and Wagner,
805 T.: Tropospheric BrO column densities in the Arctic derived from satellite: retrieval and comparison to ground-based measurements,
Atmospheric Measurement Techniques, 5, 2779–2807, https://doi.org/10.5194/amt-5-2779-2012, 2012.

Sihler, H., Beirle, S., Dörner, S., Gutenstein-Penning de Vries, M., Hörmann, C., Borger, C., Warnach, S., and Wagner, T.: MICRU back-
ground map and effective cloud fraction algorithms designed for UV/vis satellite instruments with large viewing angles, Atmospheric
Measurement Techniques Discussions, 2020, 1–58, https://doi.org/10.5194/amt-2020-182, 2020.

810 Simpson, W. R., von Glasow, R., Riedel, K., Anderson, P., Ariya, P., Bottenheim, J., Burrows, J., Carpenter, L. J., Frieß, U., Goodsite, M. E.,
Heard, D., Hutterli, M., Jacobi, H.-W., Kaleschke, L., Neff, B., Plane, J., Platt, U., Richter, A., Roscoe, H., Sander, R., Shepson, P., Sodeau,
J., Steffen, A., Wagner, T., and Wolff, E.: Halogens and their role in polar boundary-layer ozone depletion, Atmospheric Chemistry and
Physics, 7, 4375–4418, https://doi.org/10.5194/acp-7-4375-2007, 2007.

Surl, L., Roberts, T., and Bekki, S.: Observation and modelling of ozone-destructive halogen chemistry in a passively degassing volcanic
815 plume, Atmospheric Chemistry and Physics, 21, 12 413–12 441, https://doi.org/10.5194/acp-21-12413-2021, 2021.

Textor, C., Graf, H.-F., Timmreck, C., and Robock, A.: Emissions from volcanoes, in: Emissions of Atmospheric Trace Compounds,
edited by Granier, C., Artaxo, P., and Reeves, C., vol. 18 of *Advances in Global Change Research*, pp. 269–303, Springer Netherlands,
https://doi.org/10.1007/978-1-4020-2167-1_7, 2004.

Thalman, R. and Volkamer, R.: Temperature dependent absorption cross-sections of O2–O2 collision pairs between 340 and 630 nm and at
820 atmospherically relevant pressure, Phys. Chem. Chem. Phys., 15, 15 371–15 381, https://doi.org/10.1039/C3CP50968K, 2013.

Theys, N., Roozendael, M. V., Dils, B., Hendrick, F., Hao, N., and Mazière, M. D.: First satellite detection of volcanic bromine monoxide
emission after the Kasatochi eruption, Geophysical Research Letters, 36, https://doi.org/10.1029/2008GL036552, 2009.

Theys, N., Van Roozendael, M., Hendrick, F., Yang, X., De Smedt, I., Richter, A., Begoin, M., Errera, Q., Johnston, P. V., Kreher, K., and
De Mazière, M.: Global observations of tropospheric BrO columns using GOME-2 satellite data, Atmospheric Chemistry and Physics,
825 11, 1791–1811, https://doi.org/10.5194/acp-11-1791-2011, 2011.

Theys, N., De Smedt, I., van Gent, J., Danckaert, T., Wang, T., Hendrick, F., Stavrakou, T., Bauduin, S., Clarisse, L., Li, C., Krotkov, N., Yu, H., Brenot, H., and Van Roozendael, M.: Sulfur dioxide vertical column DOAS retrievals from the Ozone Monitoring Instrument: Global observations and comparison to ground-based and satellite data, Journal of Geophysical Research: Atmospheres, 120, 2470–2491, https://doi.org/10.1002/2014JD022657, 2015.

830 Theys, N., De Smedt, I., Yu, H., Danckaert, T., van Gent, J., Hörmann, C., Wagner, T., Hedelt, P., Bauer, H., Romahn, F., Pedergnana, M., Loyola, D., and Van Roozendael, M.: Sulfur dioxide retrievals from TROPOMI onboard Sentinel-5 Precursor: algorithm theoretical basis, Atmospheric Measurement Techniques, 10, 119–153, https://doi.org/10.5194/amt-10-119-2017, 2017.

Thomas, W., Erbertseder, T., Ruppert, T., Roozendael, M. V., Verdebout, J., Balis, D., Meleti, C., and Zerefos, C.: On the Retrieval of Volcanic Sulfur Dioxide Emissions from GOME Backscatter Measurements, Journal of Atmospheric Chemistry, 50, 295–320, 835 https://doi.org/10.1007/s10874-005-5544-1, 2005.

Valks, P., Loyola, D., Hao, N., and Rix, M.: Algorithm Theoretical Basis Document for GOME-2 Total Column Products of Ozone, Minor Trace Gases, and Cloud Properties, techreport, Deutsches Zentrum für Luft und Raumfahrt, Oberpfaffenhofen, Germany, 2009.

van Geffen, J., Eskes, H. J., Boersma, K. F., and Veefkind, J. P.: TROPOMI ATBD of thetotal and tropospheric NO2 data products, resreport, KNMI, https://sentinel.esa.int/documents/247904/2476257/Sentinel-5P-TROPOMI-ATBD-NO2-data-products, report S5P-KNMI- 840 L2-0005-RP, 2021.

van Roozendael, M. and the Sentinel 5 Verification team: Sentinel 5 verification report.

Vandaele, A. C., Hermans, C., Simon, P. C., Carleer, M., Colin, R., Fally, S., Merienne, M. F., Jenouvrier, A., and Coquart, B.: Measurements of the NO$_2$ absorption cross-section from $42\,000\,\mathrm{cm}^{-1}$ to $10\,000\,\mathrm{cm}^{-1}$ (238-1000 nm) at 220 K and 294 K, Journal of Quantitative Spectroscopy and Radiative Transfer, 59, 171 – 184, https://doi.org/10.1016/S0022-4073(97)00168-4, atmospheric Spectroscopy Applications 845 96, 1998.

Veefkind, J. P., Aben, I., McMullan, K., Förster, H., de Vries, J., Otter, G., Claas, J., Eskes, H. J., de Haan, J. F., Kleipool, Q., van Weele, M., Hasekamp, O., Hoogeveen, R., Landgraf, J., Snel, R., Tol, P., Ingmann, P., Voors, R., Kruizinga, B., Vink, R., Visser, H., and Levelt, P. F.: TROPOMI on the ESA Sentinel-5 Precursor: A GMES mission for global observations of the atmospheric composition for climate, air quality and ozone layer applications, Remote Sensing of Environment, 120, 70–83, https://doi.org/10.1016/j.rse.2011.09.027, 2012.

850 Vogel, L., Sihler, H., Lampel, J., Wagner, T., and Platt, U.: Retrieval interval mapping: a tool to visualize the impact of the spectral retrieval range on differential optical absorption spectroscopy evaluations, Atmospheric Measurement Techniques, 6, 275–299, https://doi.org/10.5194/amt-6-275-2013, 2013.

von Glasow, R.: Atmospheric chemistry in volcanic plumes, Proceedings of the National Academy of Sciences, 107, https://doi.org/10.1073/pnas.0913164107, 2010.

855 Wagner, T. and Platt, U.: Satellite mapping of enhanced BrO concentrations in the troposphere, Nature, 395, 486–490, https://doi.org/10.1038/26723, 1998.

Wagner, T. and the Sentinel 4 Verification team: Sentinel 4 verification report.

Wagner, T., Beirle, S., and Deutschmann, T.: Three-dimensional simulation of the Ring effect in observations of scattered sun light using Monte Carlo radiative transfer models, Atmospheric Measurement Techniques, 2, 113–124, https://doi.org/10.5194/amt-2-113-2009, 860 2009.

Warnach, S.: Bromine monoxide in volcanic plumes - A global survey of volcanic plume composition and chemistry derived from Sentinel-5 Precursor/TROPOMI data, Ph.D. thesis, Heidelberg University, https://doi.org/10.11588/HEIDOK.00031910, 2022.

Warnach, S., Bobrowski, N., Hidalgo, S., Arellano, S., Sihler, H., Dinger, F., Lübcke, P., Battaglia, J., Steele, A., Galle, B., Platt, U., and Wagner, T.: Variation of the BrO/SO$_2$ Molar Ratio in the Plume of Tungurahua Volcano Between 2007 and 2017 and Its Relationship to Volcanic Activity, Frontiers in Earth Science, 7, 132, https://doi.org/10.3389/feart.2019.00132, 2019.

865